Foveated Near-Eye Display Using Computational Holography

by

Ali Cem

A Dissertation Submitted to the
Graduate School of Sciences and Engineering
in Partial Fulfillment of the Requirements for
the Degree of

Master of Science

in

Electrical and Electronics Engineering

KOÇ ÜNİVERSİTESİ

February 2020

Foveated Near-Eye Display Using Computational Holography

Koç University
Graduate School of Sciences and Engineering
This is to certify that I have examined this copy of a master's thesis by

Ali Cem

and have found that it is complete and satisfactory in all respects,
and that any and all revisions required by the final
examining committee have been made.

Committee Members:

Prof. Dr. Hakan Ürey (Advisor)

Assoc. Prof. Onur Ferhanoğlu

Asst. Prof. Mehmet Cengiz Onbaşlı

Date: 25.02.2020

ABSTRACT

Foveated Near-Eye Display Using Computational Holography
Ali Cem
Master of Science in Electrical and Electronics Engineering
February 25, 2020

Augmented reality (AR) displays are attracting more and more attention due to their potential in industrial, medical and consumer-level applications. The ability of embedding computer-generated information with the physical world seamlessly is unique to AR displays in glass-like form factor, which is the reason why they are considered the next-generation of display devices. Increasing the field-of-view (FOV) while providing viewing comfort and true 3D vision are the most important challenges in state-of-the-art AR display design.

Computational holography is the only technology that can offer true 3D with all the required depth cues. Holographic near-eye displays (HNED) can provide continuous depth planes with the correct accommodation for a comfortable 3D experience. Existing approaches for HNEDs have small FOV and exit pupil size, which are limited by the number of pixels on the spatial light modulator. As an example, conventional holographic head-worn display architectures are limited to about 20×10 degrees FOV using a 4K resolution SLM panel and have fixed FOV.

Dynamic foveated displays with a steerable FOV across the visual field are desired. Proposed architectures require multiple moving components, which are not practical for head-worn displays due to speed, size, and power requirements. We present a new optical architecture that can overcome those limitations and substantially extend the FOV supported by the SLM. Our architecture automatically follows the gaze of the viewer’s pupil without any moving parts. Moreover, it mimics human vision by providing varying resolution across the FOV resulting in better utilization of the available space-bandwidth product of the SLM.

We achieved 28×28 degrees instantaneous FOV within an extended FOV of 60×40 degrees using a 4K SLM, effectively providing a total enhancement of >3× in instantaneous FOV area, >10× in extended FOV area. Furthermore, we have developed a novel hologram computation algorithm for the display and developed a software-based hologram correction procedure that can correct for undesired aberrations. Computer-generated holograms were used to provide 3D depth cues such as focus blur within the instantaneous FOV.

ÖZET

Holografik ve Foveated Göze Yakın Ekran
Ali Cem
Elektrik ve Elektronik Mühendisliği, Yüksek Lisans
25 Şubat 2020

Artırılmış gerçeklik (AG) ekranları endüstriyel, tıbbi ve kullanıcı seviyesi uygulamalardaki potansiyelleri sebebiyle gittikçe daha fazla ilgi çekmekteler. Bilgisayarlar tarafından oluşturulmuş içerikler yardımıyla gerçek dünyanın zenginleştirilebilmesi gözlük şeklindeki AG ekranlara has bir özelliktir ve bu sebeple de bu teknoloji geleceğin ekran teknolojisi olarak görülmektedir. Günümüzde AG ekran tasarımındaki en önemli problem kullanım rahatlığını bozmadan ve gerçek 3 boyutlu görüntü hissini koruyarak geniş görüntü açıları elde edebilmektir.

Gerçek 3 boyut deneyimini ve derinlik hissini sağlayabilen tek teknoloji holografidir. Holografik göze yakın ekranlar (HNED) sürekli derinlik algısını ve doğru odaklamayı sağlayarak konforlu bir 3 boyutlu deneyim vaat ederler. Günümüzde var olan HNED'ler kullanılan spatial light modulatorların (SLM) piksel sayılarının düşük olması sebebiyle dar görüntü açılarına ve küçük görüntü pencerelerine sahiptirler. Örnek olarak yaygın HNED mimarilerinde 4K SLM kullanılarak elde edilebilecek görüş açısı 20×10 derecedir.

Dinamik olarak görüş penceresi hareket ettirilebilen foveated ekranlar kullanılarak HNED'lerin sorunları çözülebilir. Literatürdeki mimariler hareketli parçalar içermektedir. Hareketli parçaların beraberinde getirdiği hız, boyut ve elektriksel güç kısıtlamaları sebebi ile bu mimariler pratik çözümler değillerdir. Geliştirdiğimiz yeni optik mimari bu kısıtlamaları aşarak geniş görüş açılı HNED'lerin önünü açmaktadır. Yeni mimarimiz kullanıcının baktığı yere göre değişen göz bebeği konumunu hareketli parçalar olmadan kendiliğinden takip etmektedir. Buna ek olarak görüş açısı içerisindeki görüntünün çözünürlüğü insan gözünün optik özelliklerine paralel olarak merkezden kenarlara gidildikçe azalmaktadır ve böylece SLM tarafından sunulan konum – bant-genişliği çarpımı daha efektif kullanılmaktadır.

Yeni optik mimari kullanılarak deneysel olarak 28×28 derecelik anlık görüş açısına ve 60×40 derecelik dinamik görüş açısına 4K SLM'ler ile ulaşıldı. Geçmişteki HNED'lere göre anlık görüş açısında 3 kattan fazla ve dinamik görüş açısında 10 kattan fazla iyileştirme yapıldı. Buna ek olarak optik tasarıma özel bir hologram hesaplama algoritması geliştirildi. Hesaplanan hologramlar kullanılarak görüntü kalitesi geliştirildi ve 3 boyutlu derinlik algısı oluşturuldu.

ACKNOWLEDGEMENT

I wish to express my sincere appreciation to my supervisor, Professor Hakan Ürey, who has guided and encouraged me throughout my master's studies. In addition to his vast knowledge and experience in the field optics, I was especially inspired by his intellectual curiosity and enthusiasm for his research. I consider myself very fortunate that I had the opportunity of working with him.

Next, I would also like to express my gratitude to Prof. Onur Ferhanoğlu and Prof. Mehmet Cengiz Onbaşlı for accepting to be part of my thesis defense committee and their invaluable feedback and insight.

I wish to acknowledge all OML members I had the privilege of working with for their constant support and comradery. I would especially like to thank Dr. Erdem Ulusoy and Dr. Mehmet Kıvanç Hedili for their contributions to my research as well as the good times and fond memories.

Finally, I would not be able to complete this thesis without the endless support of my family, my friends, and Selen, who not only kept me going but also directly contributed to my thesis. I would like to thank them all for believing in me and motivating me to try my hardest and be the best version of myself.

Table of Contents

LIST OF FIGURES

1 INTRODUCTION

1.1 Head-Worn Displays Overview

Head-worn displays (HWDs) have been gathering more and more attention over the last decade, especially due to the increasing popularity of augmented reality and virtual reality applications [1]. There is large interest in both consumer-level products, such as Microsoft’s HoloLens [2] and Magic Leap 1 [3], and military-level products. One of the major limitations of current HWDs is the requirement of additional relay optics [4]. Since the human eye cannot focus directly on a near-to-eye microdisplay, which are located at a distance closer than the near point of the eye, it is necessary to image the microdisplay at a plane further away from the eye. Achieving this goal is especially challenging for a large FOV, as correcting the associated aberrations and distortions require complex optics. Therefore, the consumer-level products suffer from low field-of-view (FOV), which is a consequence of using compact optics for good form factor, and the latter suffers from high costs and bulkiness of the optics. Furthermore, the majority of HWDs are fixed focus stereoscopic systems [5], which result in a mismatch between the accommodation (focus) and vergence (rotation of the eyes to maintain single binocular vision) responses and inevitably leads to viewing discomfort [6][7]. Integral imaging or pinhole-based HWDs have been attempted, but both solutions achieve reduced visual discomfort with a decrease in resolution [8]. Another effort in overcoming the vergence-accommodation conflict is to have multiple focus distances made possible by either incorporating moving optical elements or using lenses with variable focal lengths in combination with time-multiplexing schemes, both of which result in a decrease in the FOV [9].

Figure 1.1. State-of-the-art consumer-level HWDs. Both Microsoft's HoloLens [2] and Magic Leap's Magic Leap 1 [3] are successful products in the AR industry.

Holographic HWDs, on the other hand, show computer generated holograms (CGHs) with the correct perspective and all the natural depth cues to each eye by emulating the wavefront pattern that would be emitted from the displayed 3D objects [10][11]. As a result, the user can focus directly on the gazed 3D object, eliminating the discomfort caused by the vergence-accommodation conflict. In holographic HWDs, CGHs are typically displayed on phase-only spatial light modulators (SLMs) [12]. The need for relay optics is not present for such displays, since the SLM can be imaged to an arbitrary distance away from the eye [13].

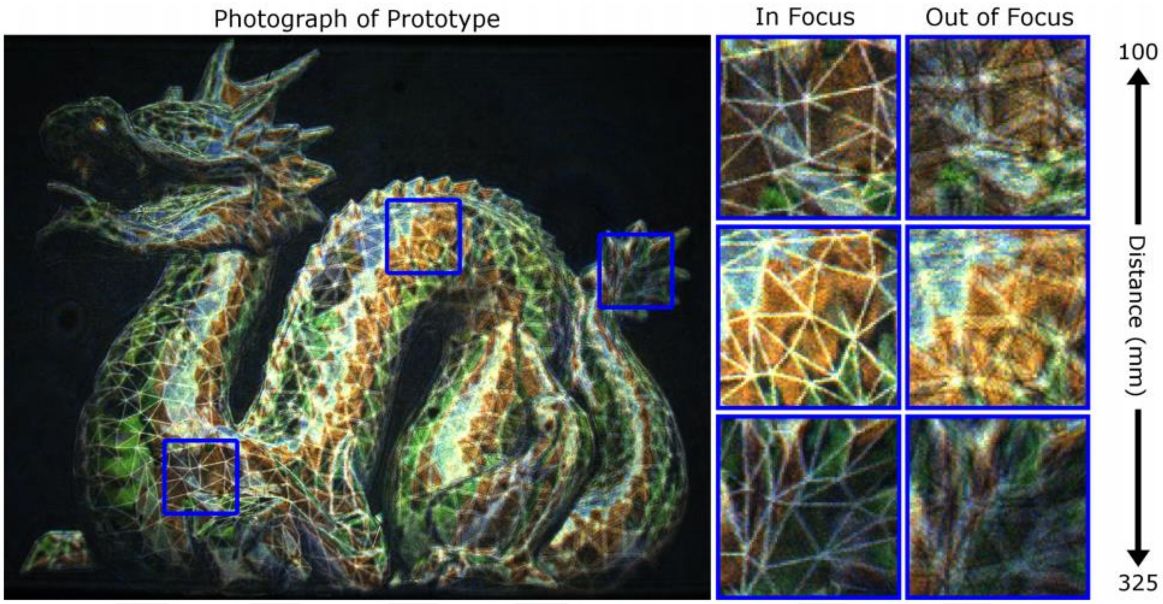

Figure 1.2. Full-color image with all natural depth cues generated by a holographic near-eye display [11].

Most holographic displays have liquid-crystal-on-silicon (LCoS) SLMs, as they can modulate amplitude, phase or polarization of the incident light, although not simultaneously. As the name implies, liquid crystal pixels are located on a silicon electronics, which can be electrically addressed to modulate the incoming light wave. The main advantage of reflective LCoS SLMs are that they are able to provide high brightness along with >2000:1 contrast in addition to their modulation capabilities. An alternative microdisplay for holographic setups is the Digital Micromirror Device (DMD), but its modulation capacity is limited. Regardless of the microdisplay used, it is illuminated by a point light source, which generates a spatially coherent wave. The microdisplay modulates the illumination wave using the CGH, which is then relayed to the eye pupil eventually forming an image on the retina. The CGH is calculated to obtain the correct ray angles for the object wave reaching the eye, which eliminates the need for bulky aberration-correcting optics.

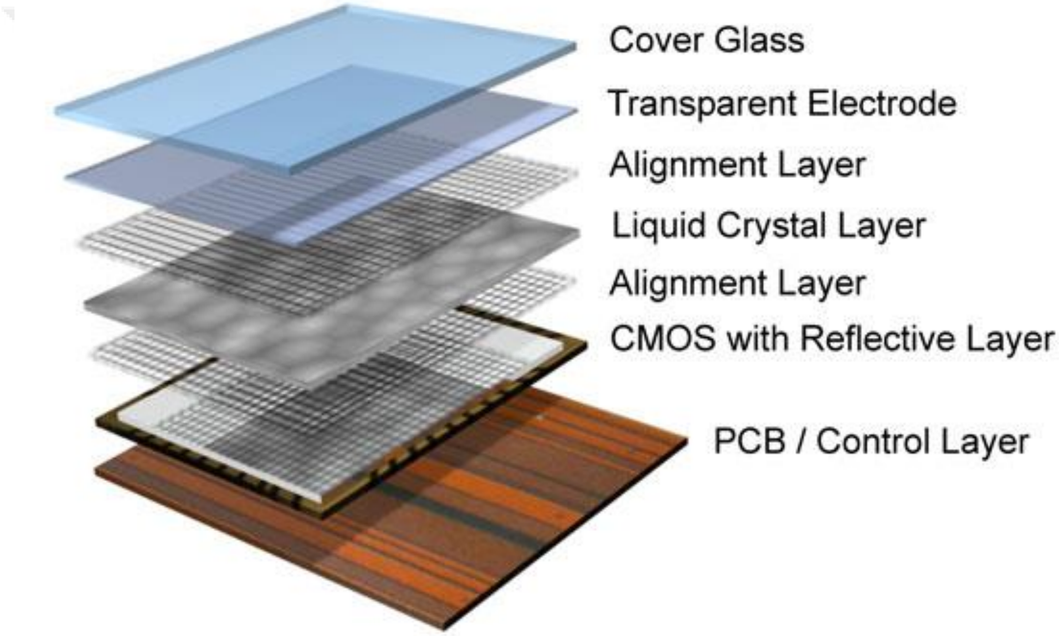

Figure 1.3. Cross-sectional view of a typical reflective LCoS SLM. Three monochromatic images for the primary colors (RGB) are displayed one after the other for full-color image generation [14].

Despite their great potential, current holographic HWDs suffer from field-of-view and eyebox (exit pupil) limitations, due to the limited pixel counts of currently available SLMs. Total pixel count of the SLM puts an upper limit on the space-bandwidth product (SBP) of the system [15][16][17][18]. To alleviate the SBP limitations, holographic displays can utilize pupil tracking and deliver the object waves through two small eyeboxes around the eye pupil, which maximizes the FOV attainable from the system [19]. State-of-the-art SLMs can have resolutions of up to 4K (3840 horizontal and 2160 vertical pixels), a display designed with such an SLM would have a limited SBP (= product of FOV and eyebox size) of 100 deg.mm in the horizontal axis. As an example, one can obtain a FOV of 20 degrees and an eyebox size of 5 mm. A FOV of 20 degrees is small for a true AR experience and a 5 mm static eyebox is also small for a comfortable viewing experience using a binocular HWD [20]. In order to match human vision capabilities, one might desire a FOV of 80 degrees and an eyebox size of 15 mm, which will require an SLM with pixel count that is in the order of 50,000 pixels in the horizontal axis (more than gigapixels in total). Such an SLM is beyond the capabilities of current technology and would be overkill from the system design perspective. Various methods have been attempted to increase the eyebox size and the FOV simultaneously with state-of-the-art SLMs, including time multiplexing [21][22] and using multiple SLMs for spatial multiplexing [23][24][25]. Despite their advantages over using a single SLM, these approaches result in complex and high-cost systems.

Since it is not currently possible to rival the FOV of human vision using holographic displays, one solution is to implement a foveated display where only the CGH for the gazed object is being generated and the peripheral image is displayed with a low-resolution microdisplay [19]. Another possibility is to combine a travelling microdisplay with a wide field-of-view peripheral display and enable natural focus depth using either a light field or a multifocal/varifocal approach [26]. Various methods have been attempted to steer the FOV from one region to another, which generally involve utilizing motorized optical components. Such solutions suffer from actuator size and synchronization issues between multiple dynamic elements, as it is not possible to steer the FOV with a single dynamic component.

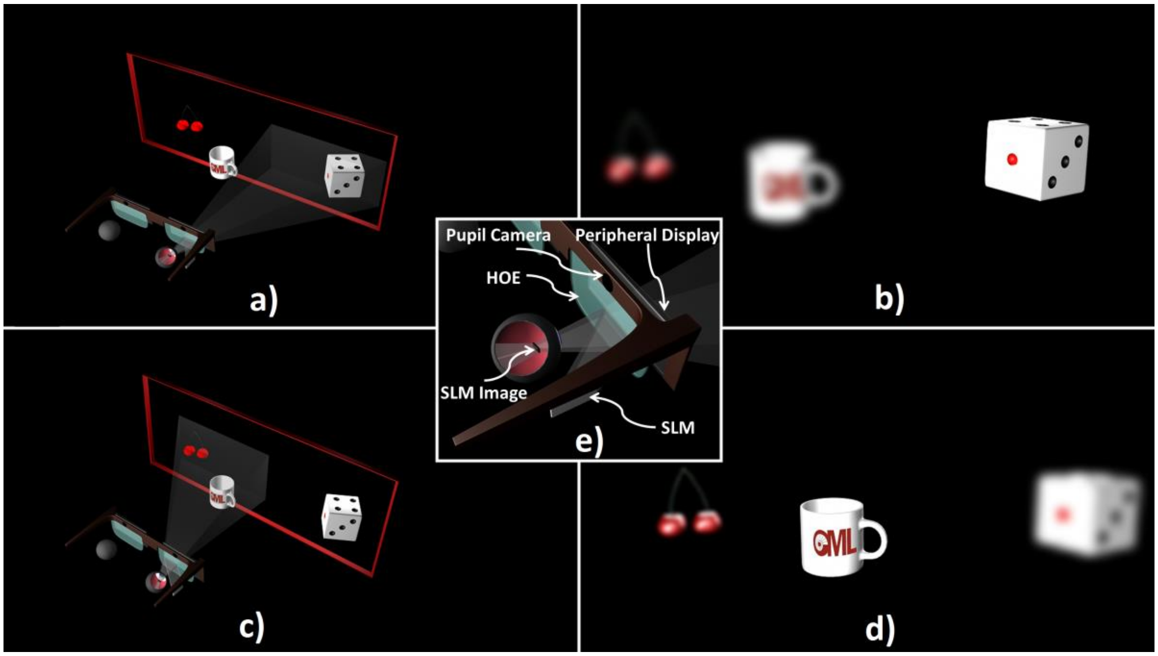

Figure 1.4. Foveated holographic display with the eye-centric design concept in eyeglass format. **a)** Red box shows the total FOV that can be delivered by the AR display. Within the FOV, an SLM is used to deliver high-resolution holographic images to the fovea. The peripheral content is delivered by a low-resolution microdisplay (e.g., micro-LED or OLED on transparent substrate) that can be placed on the eyeglass frame. **b)** The high-resolution holographic image that is projected to the fovea appears sharp and the peripheral image appears blurred. **c)** The eye-centric design ensures that the SLM image follows the fovea for all gaze directions by imaging the SLM to the rotation center of the eye. **d)** Eye rotations are measured in real-time with a pupil tracker to update the hologram on the SLM and content on the peripheral display accordingly. **e)** A close-up illustration of the eye-centric design.

We propose a novel optical architecture for holographic HWD where the SLM is imaged at the rotation center of the eye. In this architecture, instantaneous FOV can be steered without using any dynamic optical components. A particular implementation of such a system in eyeglasses form factor is illustrated in Figure 1.4.

1.2 Generic Hologram Computation Methods

Computer-generated holography is the technique of using numerical calculations based on wave optics to generate complex optical fields. For any given 3D scene, diffraction theory is used to compute the complex light field at a desired hologram plane, which is generally where the display (such as the SLM) is located. Then, the display can be used to generate the calculated field to produce the waveform that would have originated from the 3D scene. The reduction of dimension from the 3D object volume to the 2D hologram plane does not result in a loss of information as the 2D complex field captures the ray locations as well as the ray angles.

The most commonly encountered tool for hologram generation is the angular spectrum technique. Using this technique, the optical field at any plane of interest can be calculated by numerically propagating the wavefront given at another plane. Assuming that the known optical field travels along the z-axis and is located at the z = 0 plane, the complex field at the z = z_1 plane can be computed using the first Rayleigh-Sommerfeld formula [27]:

$$U(x,y,z_1)=\frac{z_1}{j\lambda}\int\int U(\alpha,\beta,0)\,\frac{\exp\left(\frac{j2\pi}{\lambda}\sqrt{(x-\alpha)^2+(y-\beta)^2+z_1^2}\right)}{(x-\alpha)^2+(y-\beta)^2+z_1^2}\,d\alpha\,d\beta \qquad (1)$$

This expression is often converted to the Fourier domain for ease of computation, which is given as:

$$G\left(f_x, f_y, z_1\right) = G\left(f_x, f_y, 0\right) \times \exp\left(j2\pi z_1 \sqrt{\frac{1}{\lambda^2} - f_x^2 - f_y^2}\right) \tag{2}$$

Therefore, given a 3D scene, if the complex field generated by that scene can be calculated at any plane, the angular spectrum technique enables the calculation of the field on the microdisplay using two 2D Fourier transform operations. Hologram calculation methods are classified based on the methods used to find the field generated by a 3D scene. The four most common techniques are the point-cloud-based synthesis, polygon-based synthesis, light-ray-field-based synthesis and the layer-based synthesis [28].

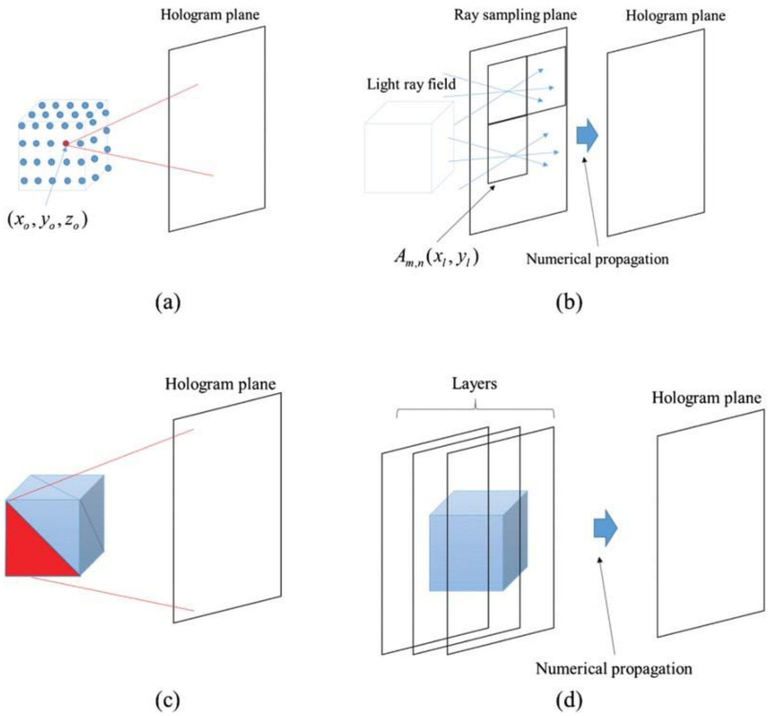

Figure 1.5. Graphical representations of the four main CGH computation techniques: **a)** Point-cloud-based method, **b)** Light-ray-field-based method, **c)** Polygon-based method, and **d)** Layer-based method [28]

In the point-cloud-based method, 3D objects are modelled as a set of point light sources. The waves generated by these sources are superposed at a reference plane, which is then propagated to the microdisplay using the angular spectrum technique. Similarly, the polygon-based method models the 3D scene as a set of polygons, of which the light field can be computed, propagated and superposed. In general, the polygon-based method is more computationally efficient for large objects compared to the point-cloud-based method, as the sampling rate for the latter is much higher than the former. Furthermore, polygon-based methods are more compatible with computer graphics technologies that are commonly used for 3D objects.

In ray-based methods such as the light-ray-field-based method, the 3D object is modelled in the form of a 4D field consisting of 2D ray locations and 2D ray angles. This 4D light field is then sampled at an intermediate plane to obtain a complex field, which can be propagated using the angular spectrum technique. Despite the degraded resolution compared to other hologram computation techniques, ray-based methods gained considerable attention as light field or integral imaging cameras enable the acquisition of ray-fields of real objects [29].

The layer-based method divides the 3D scene into a discrete number of depth layers, which are then treated as 2D images and are individually propagated using the angular spectrum technique. This method is both simple and computationally efficient, but low layer densities may lead to a layered appearance. Therefore, it is preferable to use this method when a few number of depth layers is sufficient to model the entire 3D scene.

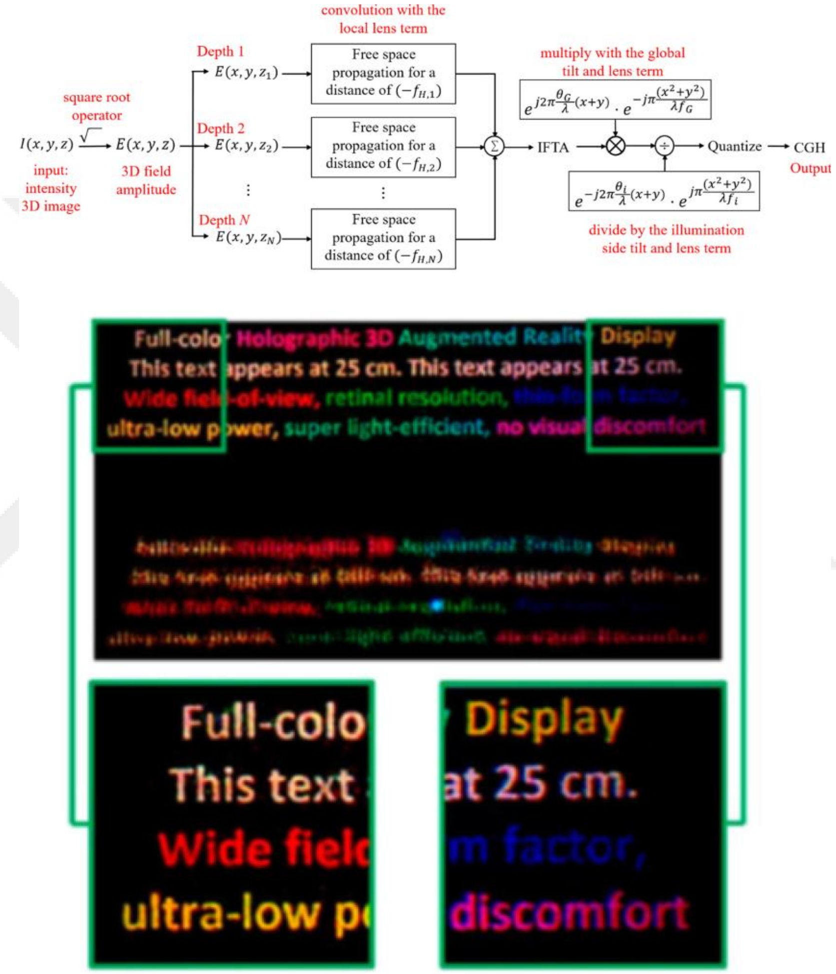

Figure 1.6. RGB hologram generated using the layer-based approach and the block diagram for its hologram computation algorithm. The text at the top is located at 25 cm and the text at the bottom is located at 100 cm, which are the two layers used in hologram calculation [13].

Note that all four common types of hologram computation are concerned mainly with the generation of a complex optical field from a given 3D scene at any location of interest, as the wave can be propagated to the SLM using the angular spectrum technique. However, this may not be straightforward if there are additional optical components between the calculated field and the SLM, especially if the components cannot be approximated using paraxial methods. The proposed eye-centric architecture for holographic HWDs suffers from this problem, which necessitates the development of a novel hologram computation algorithm.

As a final remark, due to the limitations of current SLMs in generating complex fields regardless of the method used for hologram synthesis, the calculated field must be encoded depending on the type of modulation performed by the SLM, such as amplitude-only or phase-only. The Iterative Fourier Transform Algorithm (IFTA), error diffusion and direct binary search are some of the most commonly used methods for mapping the complex holograms to a CGH suitable for the display used in the setup.

1.3 Contributions of the Thesis

Wide FOV holographic near-eye displays demand SLMs with higher pixel count due to large space-bandwidth requirements. Even 4K SLMs can only provide about 20 deg maximum FOV while maintaining a reasonable size eyebox for viewing the holograms. In our group, we developed a novel architecture named eye-centric architecture that overcomes this limitation. The eye-centric architecture places the SLM at an optical conjugate of the center of the eye, which remains conjugate with SLM even if the eye rotates to view different gaze directions. This architecture makes it possible to steer and effectively increase the FOV of a HNED significantly by moving the FOV without any moving parts.

We analyzed and derived the equations for important optical performance metrics of the novel architecture and designed the optics for the eye-centric holographic display implementation. A novel hologram calculation algorithm was developed specifically for holographic displays using the eye-centric architecture. In addition, this algorithm was designed in such a way that it can also be used to calculate holograms for any holographic display.

Using the holograms computed by our algorithm, we were able to demonstrate a steerable, holographic 28° by 28° instantaneous FOV experimentally. This is the first demonstration of a holographic foveated head-worn display without any moving parts in the literature. Furthermore, we have also shown that our novel holographic display is capable of generating full-color wide-FOV images with all natural depth cues including focus blur.

The eye-centric architecture can be exploited to build a compact HNED with eyeglasses form factor, wide and steerable FOV, and sufficient exit pupil size. Combined with a peripheral display and pupil tracker, it is possible to realize the ultimate 3D AR display with the eye-centric approach. Additionally, the hologram calculation algorithm we have developed can be applied to any optical design, regardless of complexity.

2 OPTICAL DESIGN AND ANALYSIS OF THE EYE-CENTRIC HEAD-WORN DISPLAY

2.1 Eye-centric HWD Architecture

In conventional holographic displays, steering the FOV (i.e., keeping the image centered at the fovea as the eye rotates) is not possible by just changing the CGH. As illustrated in Figure 2.1, eye rotation causes the displayed image to shift towards the peripheral vision. SLM or lenses need to be moved mechanically to bring the image onto the fovea.

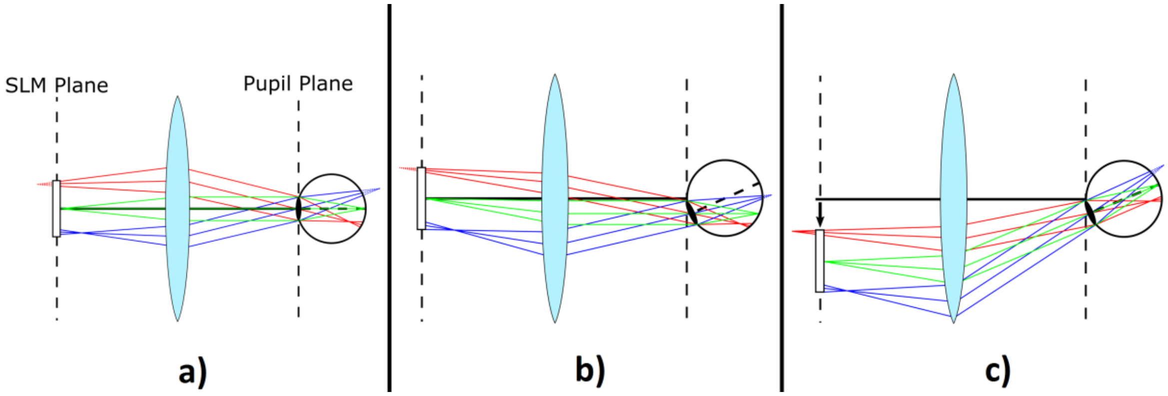

Figure 2.1. In-line diagram for conventional HWD architecture. **a)** Conventional display architecture where the SLM is imaged at the retina. **b)** If the eye rotates, the SLM image shifts to the peripheral vision. **c)** SLM movement is required to shift the image back to fovea.

Imaging the SLM at the rotation center of the eye, which we call the eye-centric design, is at the core of our proposed architecture. Since the SLM is imaged at the rotation center of the eye, changing gaze directions are handled by changing the direction of rays via CGH as illustrated in Figure 2.1. Direction of the rays is altered by adding diffractive lens terms and grating terms on the CGH without any moving components. In essence, a demagnified SLM image at the center of the eye projects the holographic image onto the fovea and the eye rotations are handled by adding tilt terms to the CGH.

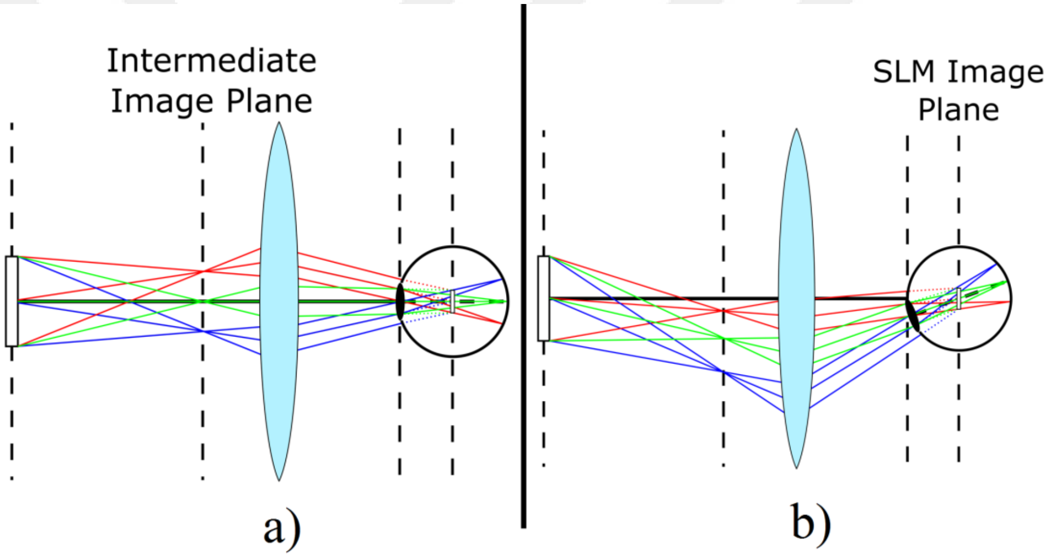

Figure 2.2. **a)** In our eye-centric design the SLM is imaged at the rotation center of the eye projects a holographic image to the retina. **b)** If the eye rotates, light from the SLM still enters through the pupil and always falls on the fovea.

Conventional displays have fixed FOV and eyebox size, therefore fixed spatial resolution across the FOV. In the eye-centric design, the eyebox size decreases towards the edges of the instantaneous FOV due to vignetting effects, which results in degrading resolution away from the foveal vision. As the instantaneous FOV follows the pupil, an extended FOV is achieved as shown in Figure 2.2.

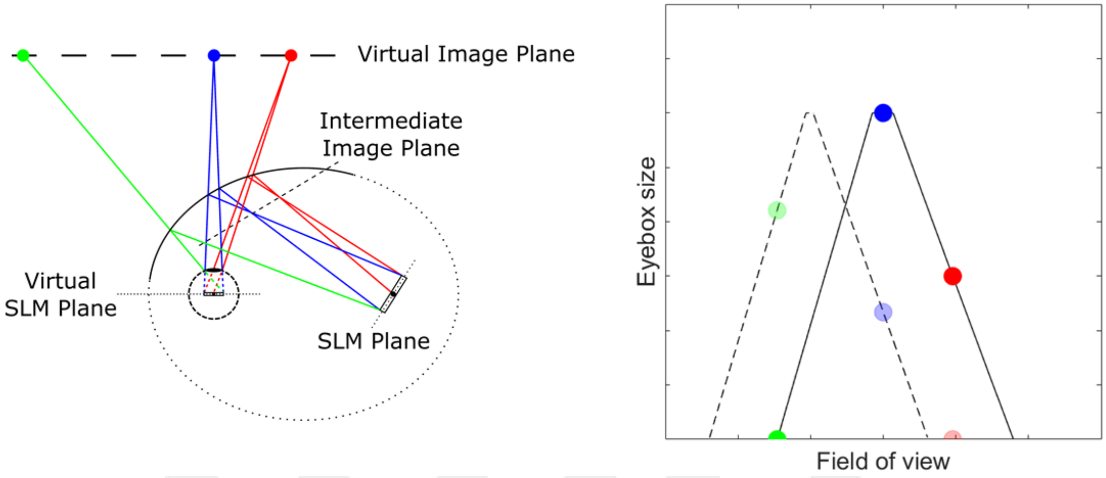

Figure 2.3. The eye-centric architecture results in a trapezoidal eyebox-FOV curve. Different virtual object points are supported by different portion of the SLM (left), which results in a degraded resolution for off-axis points. If the eye rotates, the eyebox size vs. FOV curve shifts accordingly and the resolutions associated with virtual object points are modified.

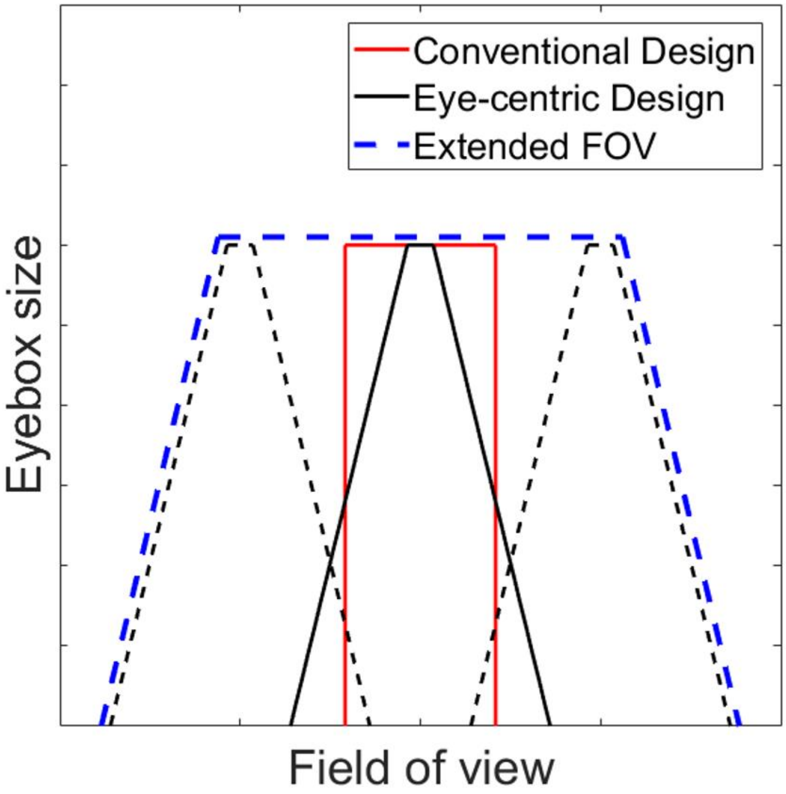

Figure 2.4. Eyebox size vs. FOV curve for conventional and eye-centric holographic displays. The ability to shift the curve results in larger extended FOV.

The eye-centric design has two major advantages compared to conventional holographic HWD architectures: i) Instantaneous FOV can be digitally steered by only modifying the CGH to follow the gaze, providing a natural foveated display with no moving parts. ii) The extended FOV is much larger than what is achievable with conventional holographic HWDs.

2.2 Optical Design and Simulations

The eye-centric design can be realized using different optical components, as illustrated from Figure 2.5 to Figure 2.7. The key point is to image the center of the SLM to the rotation center of the eye. This can be achieved by using a flat holographic optical element (HOE) in front of the eye that can be optimized for small form factor. With HOEs color correction is a challenge with wide FOV so achieving full color displays is difficult. Figure 2.6 shows an alternative design using a section of an ellipsoid as the combiner element. An SLM that is placed at one of the foci of the ellipsoid is imaged at the second focus of the ellipsoid. This is a simpler solution, but the magnification is not constant across the FOV. Additional imaging optics can be used to design a more compact system with balanced magnification as illustrated in Figure 2.7.

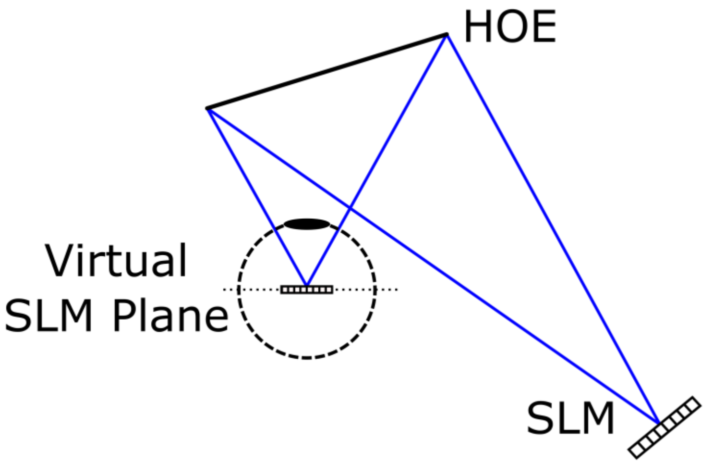

Figure 2.5. Eye-centric design can be implemented using a holographic optical element that images the SLM to the rotation center of the eye.

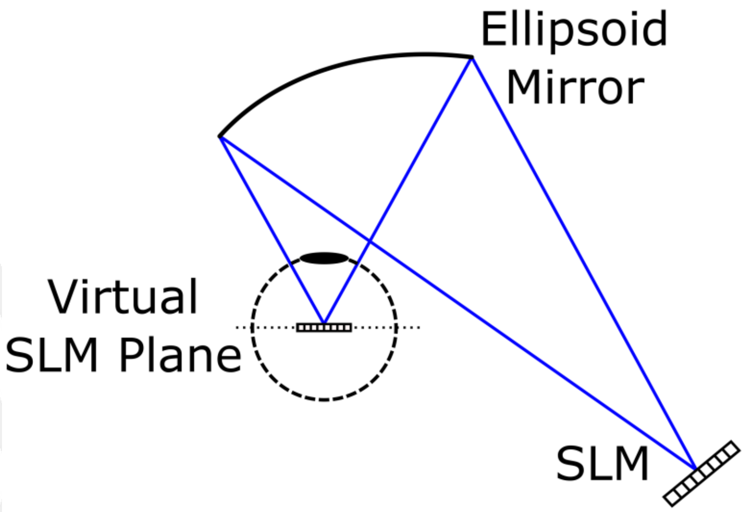

Figure 2.6. Using a section of a reflective ellipsoid is a simple alternative to HOEs, with no chromatic deviations in the design.

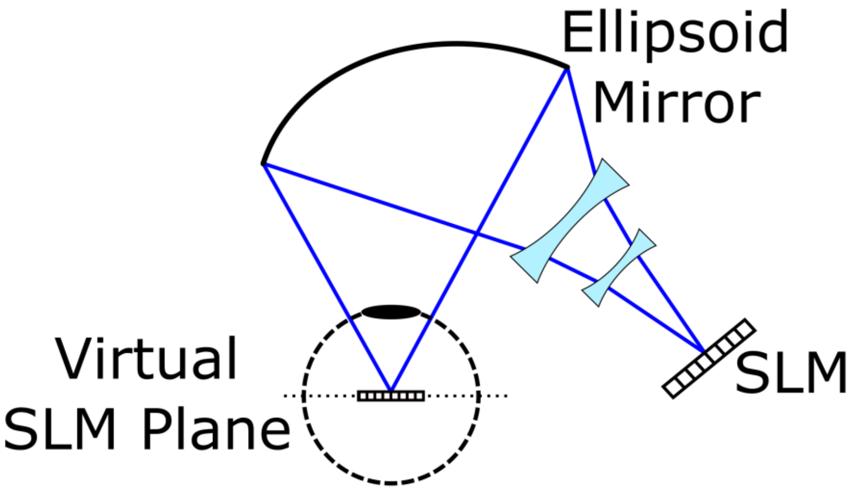

Figure 2.7. Additional optics can be used to balance the non-uniform magnification of the ellipsoid.

In their current state, commercially available SLMs introduce additional challenges that must be resolved so that our proposed eye-centric holographic HWD approach can be properly realized. The pixelated structure of LCoS SLMs results in diffraction orders of both the modulated signal beam and the unmodulated illumination beam. As the pixel sizes for commercially available SLMs are typically around 4-6 microns, the angular separation between the diffraction orders is less than 10° for visible light. The unmodulated DC beam and its replicas emerging from the SLM can be filtered out at the pupil plane by introducing an angular tilt term for the signal beam and aligning it with the middle of the DC beam and its first diffraction order. Then, by designing the illumination optics so that the unmodulated beams are focused at the pupil plane, the pupil itself can filter them out along with the replicas of the signal beam. Using the paraxial approximation, it is possible to conduct a 2D analysis that will produce useful relations between the optical design parameters of the system. Doing so, the separation between the focused spots resulting from the unmodulated beams on the pupil plane, which we call the maximum eyebox size is given by

$$EB_{max} = \frac{\lambda M r}{\Delta}, \tag{1}$$

where M is the demagnification of the imaging system for a given gaze angle, r is the distance between the center of the eye and the pupil plane, and Δ is the pixel pitch of the SLM. In practical applications, the central part of the eyebox with size equal to that of the pupil is used for the signal beam and the area close to the edges of the eyebox is reserved for noise resulting from phase encoding, which gets filtered out by the pupil. The eyebox utilization ratio η is defined to be the ratio between the pupil size EB_p and the maximum eyebox size. Under this formulation, the required demagnification for a given eyebox utilization ratio and pupil size can be found using

$$M = \frac{EB_p}{\eta} \frac{\Delta}{\lambda r} \tag{2}$$

Having found the demagnification of the optical system, the size of the SLM image W_{SLM} at the eye center can also be calculated as

$$W_{SLM} = \frac{N\Delta}{M}, \tag{3}$$

where N is the number of pixels of the SLM along the axis of interest. The size of the SLM image, the pupil size and the distance between the pupil and the eye center is sufficient to calculate the eyebox size supported by the SLM for a virtual object point at infinity. For points inside the central field-of-view FOV_c, the supported eyebox size EB_c is equal to the minimum of EB_p and W_{SLM}. EB_c decreases linearly for points outside FOV_c and reaches zero for a point on the edge of the instantaneous field-of-view FOV_i. The relations between the FOVs and the physical design parameters are given by the following equations:

$$FOV_c = \left| \frac{EB_p - W_{SLM}}{r} \right| \tag{4}$$

$$FOV_i = \frac{EB_p + W_{SLM}}{r} \tag{5}$$

The trapezoidal eyebox-FOV curve becomes triangular when the pupil size is equal to the SLM image size. The area under the curve, which is equal to the space-bandwidth product SBP can be expressed as

$$SBP = \frac{FOV_c + FOV_i}{2} EB_c = N\lambda\eta \tag{6}$$

Note that for a given SLM, while the SBPs of our novel eye-centric architecture and the conventional holographic HWD architecture are the same, the eye-centric design has a larger FOV. The main difference between the two approaches in terms of their eyebox-FOV curves is that the eyebox size is constant over the FOV for the conventional approach while the eyebox size decreases gradually near the edge of the FOV for the eye-centric approach, making it possible to have a higher instantaneous FOV without changing the eyebox size for the central FOV. The eye-centric approach provides full resolution only at the fovea and the resolution degrades towards the edges of the FOV, which is consistent with the human visual system. Therefore, the eye-centric architecture results in a more efficient utilization of the available space-bandwidth product.

Limiting the analysis to the horizontal FOV, designing for a full HD SLM with a pixel pitch of 4.5 microns and assuming a pupil size of 3 mm with an eyebox utilization ratio of 0.8, it is apparent that the conventional approach cannot have an instantaneous FOV of more than 15°. On the contrary, it is possible to reach an instantaneous FOV of 25° using the eye-centric approach.. Selecting the demagnification high enough so that the unmodulated beams and the diffraction orders are separated at the pupil plane makes the SLM image so small that the supported eyebox size is 2.8 mm even at the center of the FOV. Furthermore, the central FOV is only slightly larger than 2°, which is significantly smaller than the FOV for human central vision. In order to overcome these problems while preserving the eye-centric property of the system, an SLM with smaller pixel pitch and larger pixel count is required. Using a 4K SLM with a pixel pitch of 3.74 microns with a demagnification of 2.6 resolves all of the previously discussed issues: the central FOV exceeds 10° and the corresponding eyebox size reaches 3 mm. In addition, the overall instantaneous FOV is higher than 30°.

Smaller magnification brings larger eyebox and FOV, but high enough magnification is needed for sufficient separation of the diffraction orders, which results in a small eyebox and small FOV. Therefore, an optimum point should be selected for given SLM and desired display parameters. As seen in Figure 2.8, M = 4 gives the best trade-off.

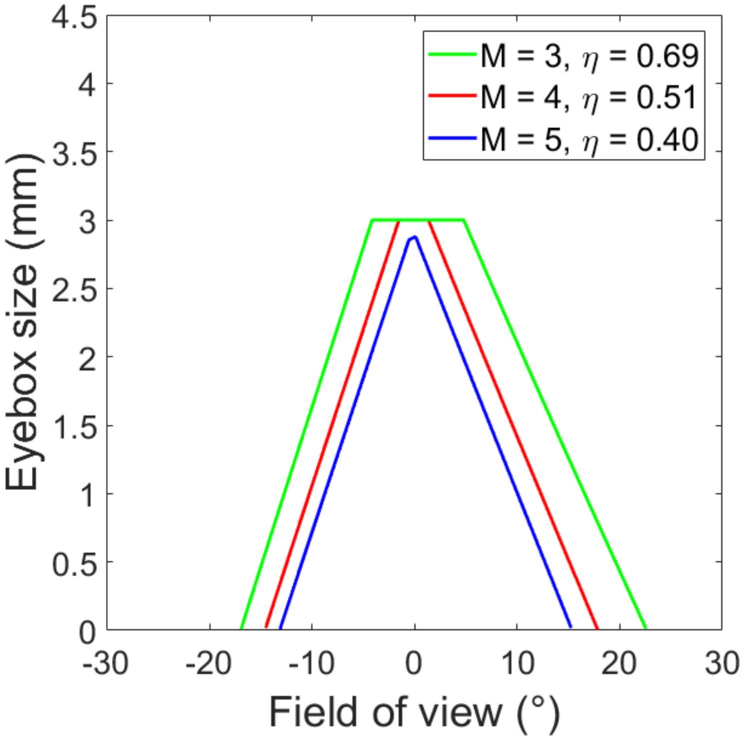

Figure 2.8. Ellipsoids with different nominal magnifications were analyzed. We chose M = 4 as it provides a good trade-off between the eyebox size and the eyebox utilization ratio η. As each point on the ellipsoid has a different focal length, the magnification across the FOV is non-uniform. This results in an asymmetrical trapezoid.

We designed and simulated the ellipsoid with M = 4 using Zemax. As seen in Figure 2.9, the instantaneous FOV varies for different gaze angles due to non-uniform magnification across the ellipsoid. Moreover, this non-uniformity introduces a significant distortion to the wavefront as seen in the spot diagram at the pupil plane in Figure 2.10, Figure 2.11, and Figure 2.12. Spot diagrams show the diffraction orders of the illumination beam for RGB colors. The clear region between the orders is the eyebox of our display. A pupil with 3 mm diameter filters out the diffraction orders so that the image can be seen clearly. Figure 2.9 show the corresponding eyebox-FOV curves for each gaze angle. Clear eyebox size decreases, hence the instantaneous FOV increases from nasal to temporal gaze angles.

Since the effective focal length is not constant on the ellipsoid, the magnification is non-uniform across the combiner surface. We defined the nominal magnification as the ratio of the distance from eye-center to ellipsoid and the distance from the ellipsoid to the center of the SLM for 0° gaze angle. This non-uniform magnification brings asymmetry to the trapezoid in eyebox size-FOV curve.

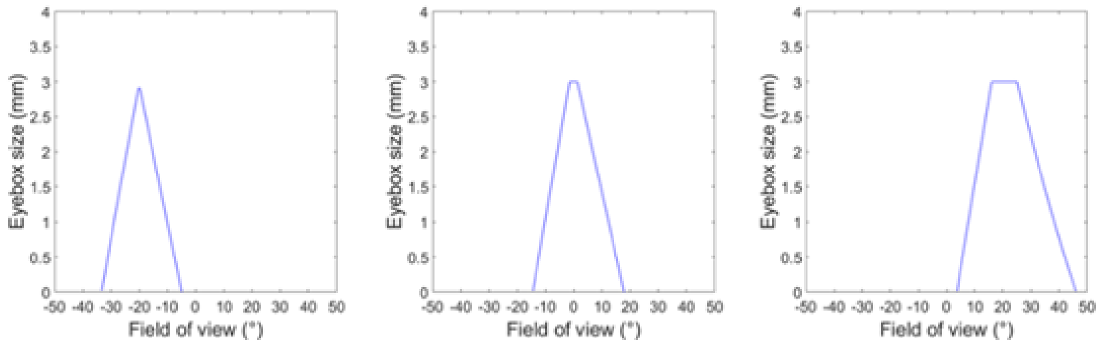

Figure 2.9. Eyebox-FOV curves obtained from the ray-based MATLAB simulation of the ellipsoid. Note that the asymmetrical trapezoid gets wider as the FOV is shifted towards the temple and narrower as the FOV is shifted towards the nasal direction.

We modeled and simulated the ellipsoid described above in Zemax as seen in Figure 2.14 to Figure 2.16. Different gaze angles from -20° to +20° are simulated. The blue rays show the central vision, red and blue rays show the edges of the instantaneous FOV. Due to the non-uniform magnification across the aperture of the ellipsoid, the instantaneous FOV varies; getting larger from nasal to temporal FOV. The full color eyeboxes for each gaze angle is shown in the corresponding figures on the right. The colors show the actual color of the diffraction orders due to the pixelated structure of the SLM. The circle in the middle shows the eye pupil with 3 mm diameter. As seen in the simulations the eyebox is sufficiently large and no diffraction orders enter the eye.

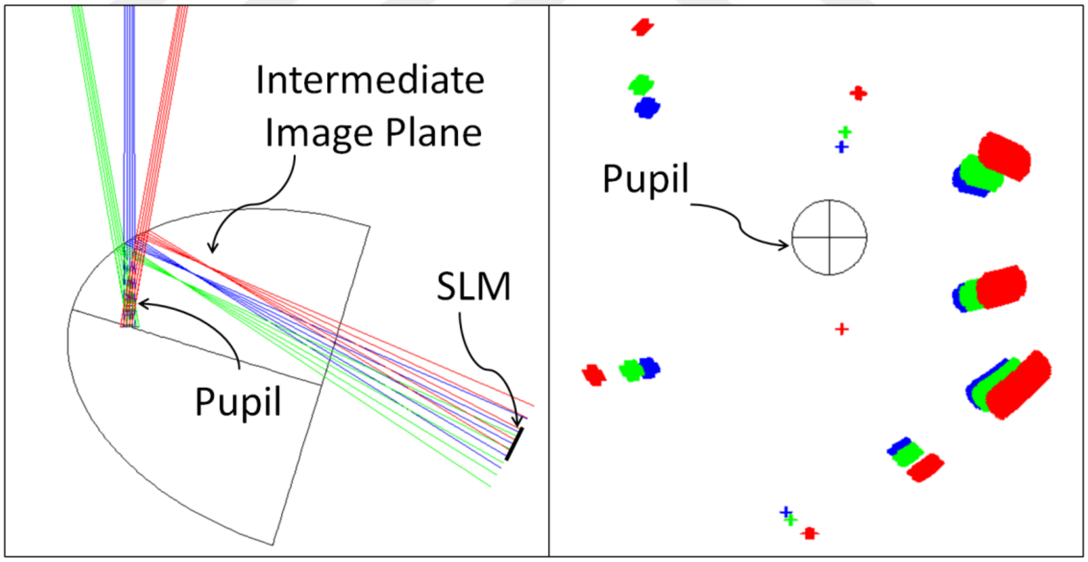

Figure 2.10. Zemax simulation of the ellipsoid as an eye-centric display implementation. On the left, the rays reaching the SLM for different object points and the intermediate image plane are shown. On the right, a 3 mm pupil in the eyebox and the diffraction orders are seen for the nominal gaze direction.

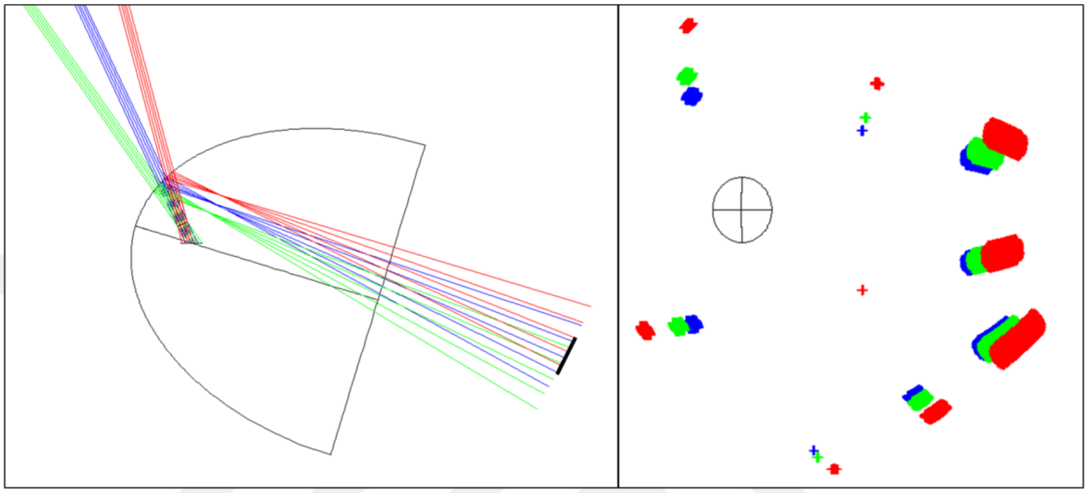

Figure 2.11. Zemax simulation of the ellipsoid for a gaze angle of -20°.

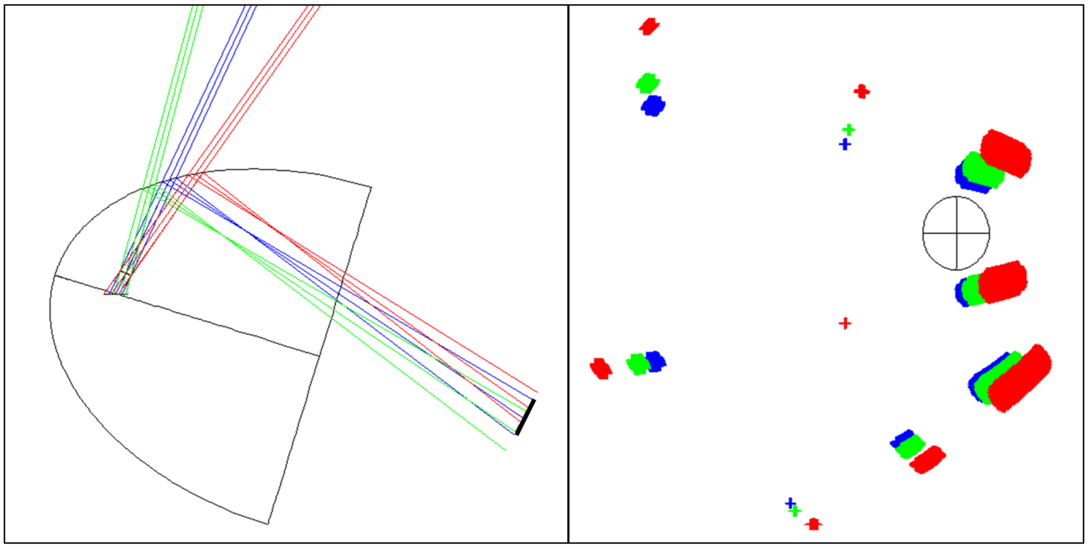

Figure 2.12. Zemax simulation of the ellipsoid for a gaze angle of +20°.

Magnification is one of the key parameters of the ellipsoid for our display. Smaller magnification brings larger eyebox and FOV, but high enough magnification is needed for sufficient separation of the diffraction orders due to the pixelated structure of the SLM, which results in a small eyebox and small FOV. Therefore, an optimum point should be selected for a given SLM and desired display parameters. In our design we chose M = 4. The magnification is defined as the inverse of the ratio of the distance from the eye center to the ellipsoid in y-direction (50 mm) and from that point to the distance to center of the SLM (200 mm) in Figure 2.13. The a, b, and c parameters of the ellipsoid are 125 mm, 86.96 mm and 86.96 mm, respectively.

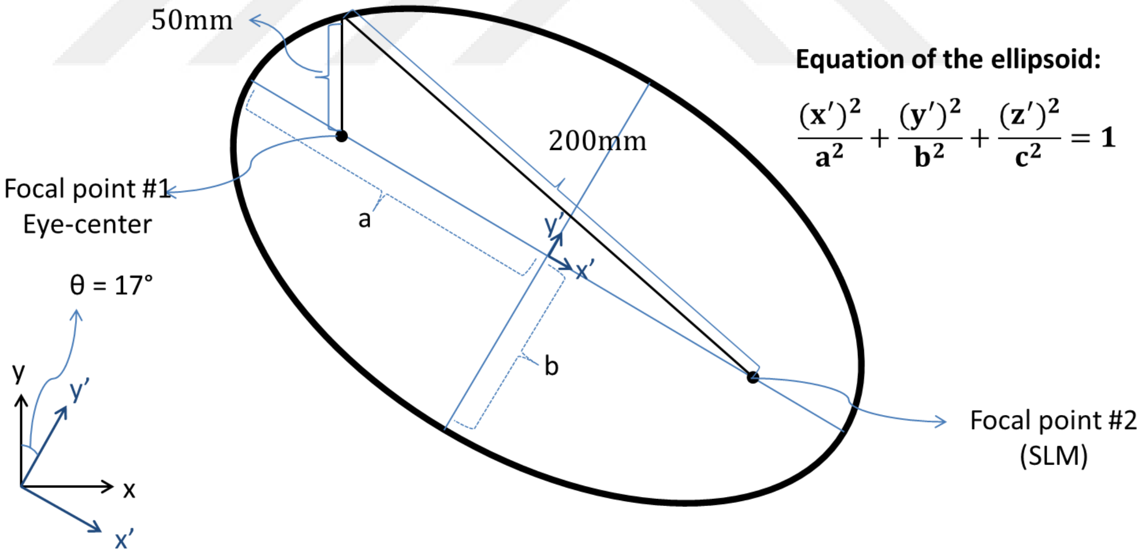

Figure 2.13. Ellipsoid parameters of our design.

We modeled and simulated the ellipsoid described above in Zemax as seen in Figure 2.14 to Figure 2.16. Different gaze angles from -25° to 25° are simulated. The blue rays show the central vision, red and blue rays show the edges of the instantaneous FOV. Due to the non-uniform magnification across the aperture of the ellipsoid, the instantaneous FOV varies; getting larger from nasal to temporal FOV. The full color eyeboxes for each gaze angle is shown in the corresponding figures on the right. The colors show the actual color of the diffraction orders due to the pixelated structure of the SLM. The circle in the middle shows the eye pupil with 3 mm diameter. As seen in the simulations the eyebox is sufficiently large and no diffraction orders enter the eye.

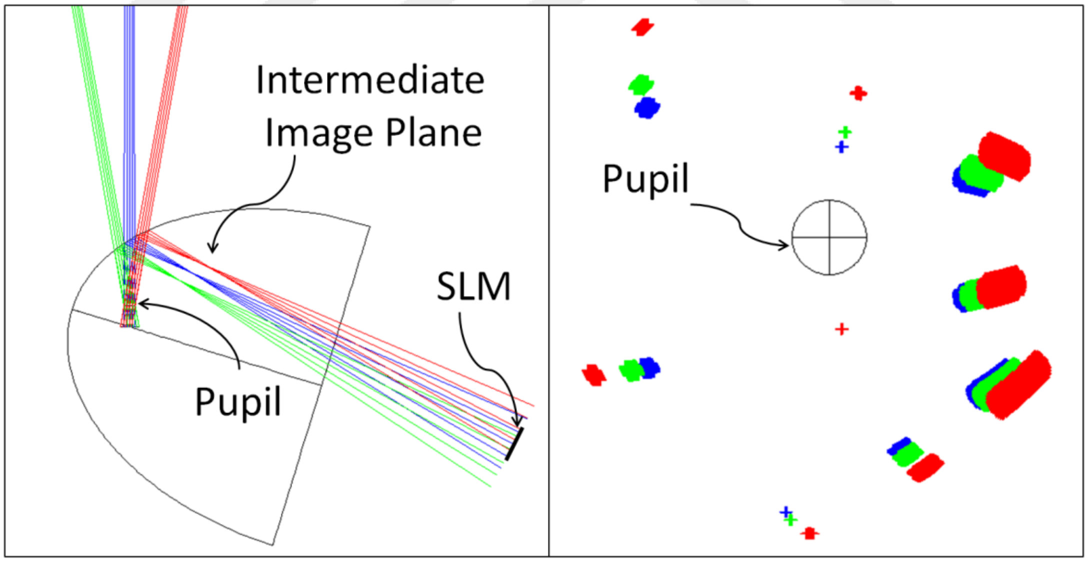

Figure 2.14. Zemax simulation of the ellipsoid as an eye-centric display implementation. On the left the rays reaching the SLM for different object points and the intermediate image plane are shown. On the right a 3mm pupil in the eyebox and the diffraction orders are seen for gaze = 0°.

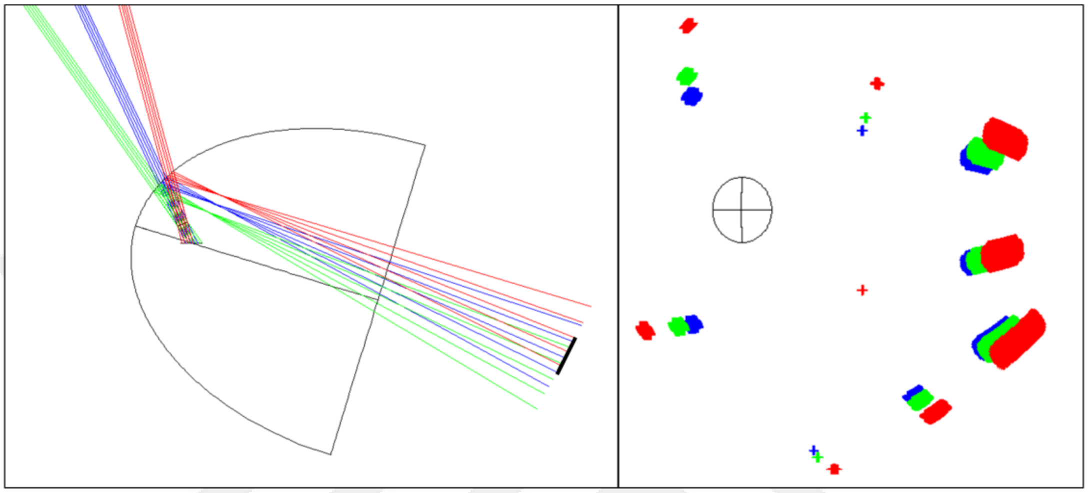

Figure 2.15. Zemax simulation for gaze = -25°.

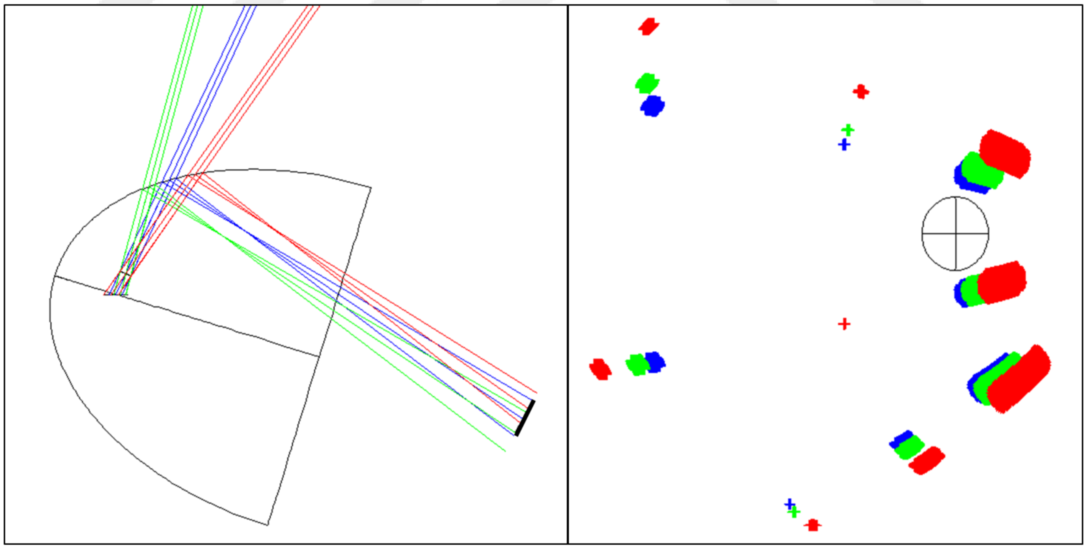

Figure 2.16. Zemax simulations for gaze = 25°.

2.3 Conclusion

The eye-centric HWD architecture was introduced. The eye-centric architecture makes it possible to move the instantaneous FOV within an extended FOV by modifying the hologram alone. As a side effect, using a single ellipsoidal mirror to realize the eye-centric design results in a trapezoidal eyebox-FOV curve, which mimics human vision. The equations for the eyebox size and the FOV were deduced for the proposed optical setup and an ellipsoid mirror was designed in ZEMAX, which has an instantaneous FOV of 25° by 25° and an eyebox size of 3 mm by 3 mm for a 4K SLM.

3 HOLOGRAM CALCULATION AND ADAPTIVE WAVEFRONT CORRECTION FOR THE HEAD-WORN DISPLAY

3.1 Hologram Calculation

Conventional CGH computation algorithms typically use the angular spectrum method to numerically propagate the optical field from a 3D scene to the hologram plane where the SLM is located [29]. Optical components used in conventional holographic HWDs such as beamsplitters or lenses are approximated using paraxial models with high accuracy, which makes it possible to use an in-line model for the entire setup. In our experimental setup using the eye-centric architecture, an off-axis ellipsoidal mirror is required to image the SLM to the eye center, which cannot be modelled as a paraxial lens due to its varying magnification across the FOV. Therefore, we have developed an algorithm based on ray tracing to calculate CGHs, where the 3D scene is considered to be a set of luminous points emitting spherical waves, similar to how the 3D scene is decomposed in the wave-propagation based methods where objects are represented by point clouds [30][31][32].

In order to compute the hologram for a point object, rays must be traced using ray tracing software back from the virtual image point to the SLM, where a 2D phase function approximating the wavefront can be fit. A 66 by 66 uniform grid of rays were emitted from the object, filling the pupil entirely. By placing a retroreflector in place of the pupil, the rays were directed back to the reflective ellipsoidal surface, which reflects them to the

SLM. The points where the rays hit the SLM are denoted by (x_{ij}, y_{ij}), where the x- and y-axis correspond to the horizontal and vertical axes passing from the center of the SLM, respectively. The angle between the ray with index ij and the x-axis is defined to be α_{ij} and the angle between the same ray and the y-axis is defined to be β_{ij}. The phase function $\phi(x,y)$ must satisfy the following conditions so that it accurately describes the wavefront on the SLM required for the reconstruction of the point object:

$$\frac{\partial}{\partial x}\phi\left(x_{ij}, y_{ij}\right) = \frac{2\pi}{\lambda}\sin\left(\alpha_{ij}\right) \tag{7}$$

$$\frac{\partial}{\partial y}\phi\left(x_{ij}, y_{ij}\right) = \frac{2\pi}{\lambda}\sin\left(\beta_{ij}\right) \tag{8}$$

Many different methods for finding such phase functions have been developed, especially in the field of optical metrology [33][34][35]. One possible way of finding such a phase function is to assume that it is in the following form:

$$\phi(x,y) \approx \phi_z(x,y) = \sum_{i=1}^{N} a_i Z_i\left(\rho(x,y), \theta(x,y)\right), \tag{9}$$

where Z_i is the Zernike polynomial with Noll index i and N is the number of Zernike polynomials used to approximate the phase function. Under this formulation, the problem of fitting a phase function is equivalent to finding N Zernike coefficients that best satisfy the phase constraints. The Zernike coefficients were computed by finding the minimum norm least squares solution to the overdetermined system. Simulations have shown that choosing $N = 10$ results in reconstruction errors less than that of a diffraction-limited optical system.

Having computed the phase function $\phi(x,y)$, the full-complex hologram for a point object is given by $H(x,y)=\sqrt{I}e^{j\phi(x,y)}$, where I denotes the optical intensity of the object. In order to compute the full-complex hologram of the entire 3D content to be displayed, one can simply treat it as a collection of points located at the centers of the voxels making up the 3D content. The full-complex hologram is then expressed as the summation of all individual point object holograms. After the full-complex hologram for the entire scene has been computed, a pixel-by-pixel multiplication with a linear phase term is required to shift the hologram to the middle point between the 0th and 1st diffraction orders, which will eventually be filtered-out by the pupil.

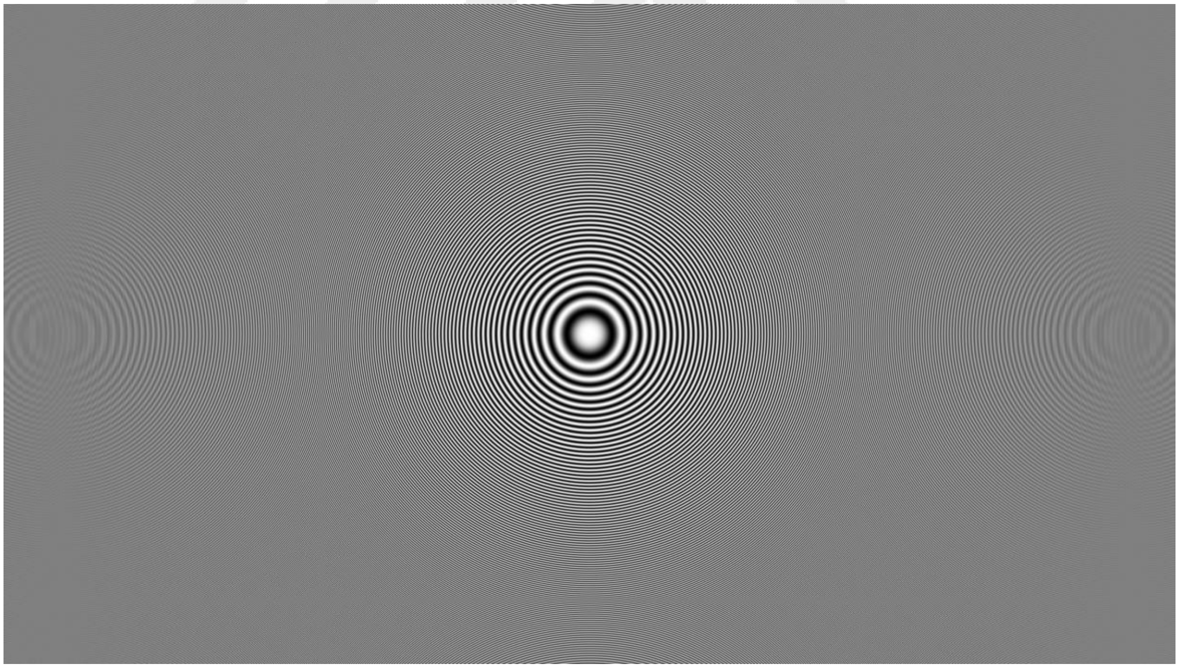

Figure 3.1. Real part of the hologram for a point on the nominal gaze direction.

As a final step, the full-complex hologram must be encoded to a phase pattern so that it can be displayed on a phase-only SLM. The complex function obtained by superposing the holograms for all virtual object points is approximated using a phase-only hologram computed using the iterative Fourier transform algorithm with 10 iterations, which is a well-known method for encoding complex CGHs into phase or amplitude CGHs [36][37].

Having computed the phase hologram, minor post-processing operations are required so that it can be displayed on the SLM. The real phase values are mapped to the 0-255 range and quantized so that they can be represented as 8-bit integers. Then, the hologram is set to be the red channel of a 24-bit FHD RGB image and the green and blue channels are set to 0, which is a requirement when working with the SLM used in the experiments.

The proposed algorithm for CGH computation includes ray tracing and surface fitting for every point on the 3D content, which results in very high computational cost. In practice, we approximated the holograms for some object points using the holograms of nearby object points to accelerate hologram calculation, which we call the zone-based approach.

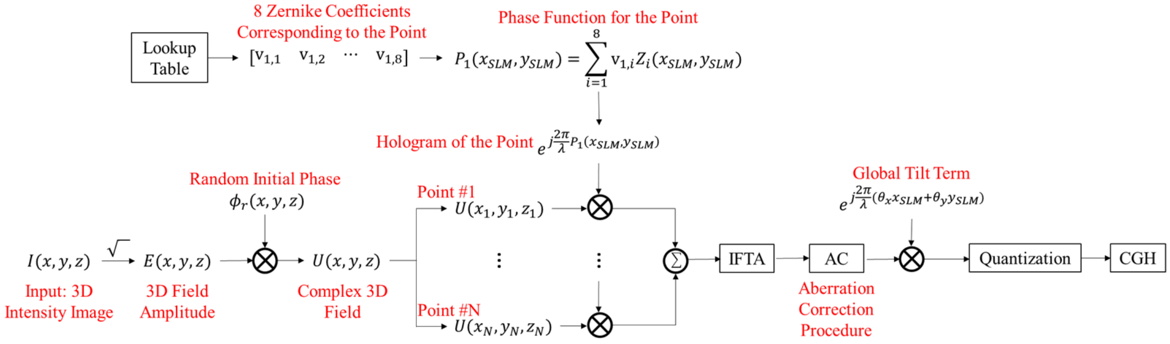

Figure 3.2. Block diagram summarizing the hologram calculation pipeline.

Using the zone-based approach, virtual object points close to each other can be grouped and approximated relatively well by only modifying the tilt terms of the corresponding Zernike polynomials for the wavefront of one of the points. We have divided the FOV into a set of zones and have only calculated to point holograms for the zone centers and the zone corners using ray tracing. Therefore, the lookup tables used in practice only consisted of the Zernike coefficients for the phase functions of less than 50 individual points. Unfortunately, it is not possible to treat the entire FOV as a single zone and use the hologram of the gaze point to generate the entire hologram since the magnification changes across the FOV. However, using a more sophisticated optical design with uniform magnification would enable such an approximation, which would result in a real-time hologram computation algorithm.

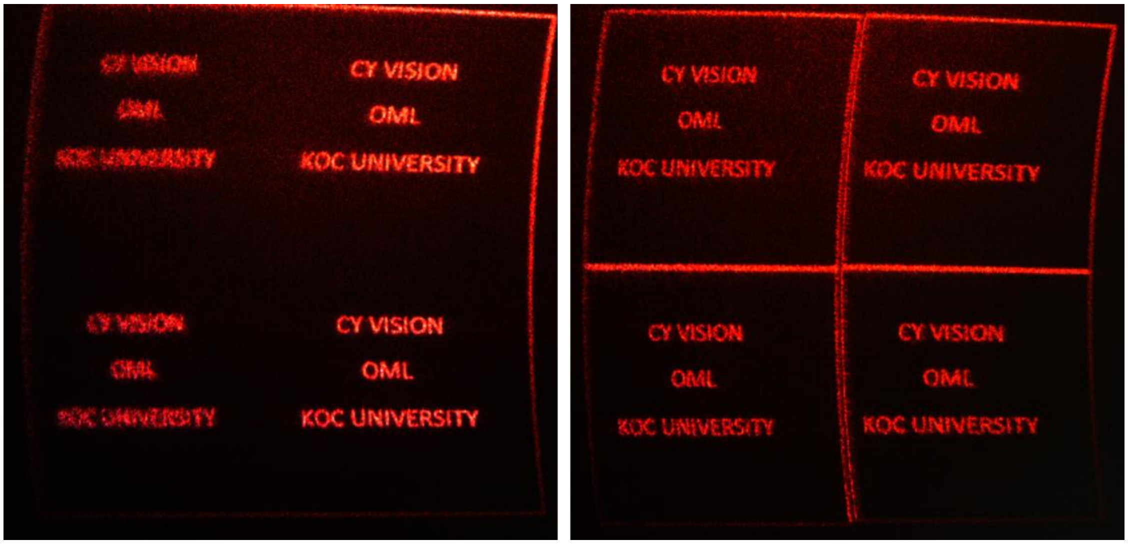

Figure 3.3. Images obtained using holograms computed with a single-zone approach (left) and a multiple-zone approach (right). A single zone is not sufficient to cover the entire FOV due to the varying magnification, which results in some portions of the image being

out of focus. On the other hand, using a 2x2 array of zones results in an image where all 4 texts appear sharp.

3.2 Adaptive Wavefront Correction

The off-axis optical system used for the holographic display makes precise alignment challenging. Furthermore, using a 3D-printed housing for the experimental setup in combination with the optical table results in relatively high tolerances for the entire system. Therefore, deviations of the experimental results from the expected outcome are inevitable, since correcting for the alignment issues together with the non-ideal behavior of the SLM is not a trivial task. In order to improve the image quality, a series of correction procedures were included in the hologram computation pipeline, which improved the experimental results significantly.

The first major issue was that the brightness was not uniform within the FOV, some regions in the FOV were much brighter than others. Observing the EB-FOV curves, it is expected that the resolution and brightness gets worse at the edges compared with the center of the FOV. However, since we are not using the maximum FOV of 28° and only using the central 20°, this effect should not be as significant a observed in the experiments. Furthermore, the experimental result indicate that the upper parts of the FOV (which are closer to the 0^{th} diffraction order) are brighter than the lower ones, which is not a result predicted by any theoretical analysis or simulation.

In order to achieve brightness uniformity, a hologram of a white square filling the entire FOV was calculated, and its image was captured with a camera. Note that the entire FOV corresponds to a 750 by 750 pixel region in the camera image. The resulting image is very noisy due to the random initial phase introduced in hologram computation, which results in speckle noise. To filter-out the noise, a non-linear filter was used to obtain an intermediate result, which can then be smoothened using a low-pass filter (Figure 3.4). Firstly, the camera image was upsampled to fit in a 2300 by 2300 pixel window. Then, the upsampled image was divided into 23 by 23 squares, each having a side length of 100 pixels. Finally, the pixel values within each square was replaced by the average pixel values of the entire square. The intermediate result was then low-pass filtered with a 2D Gaussian filter with a standard deviation of 100 pixels.

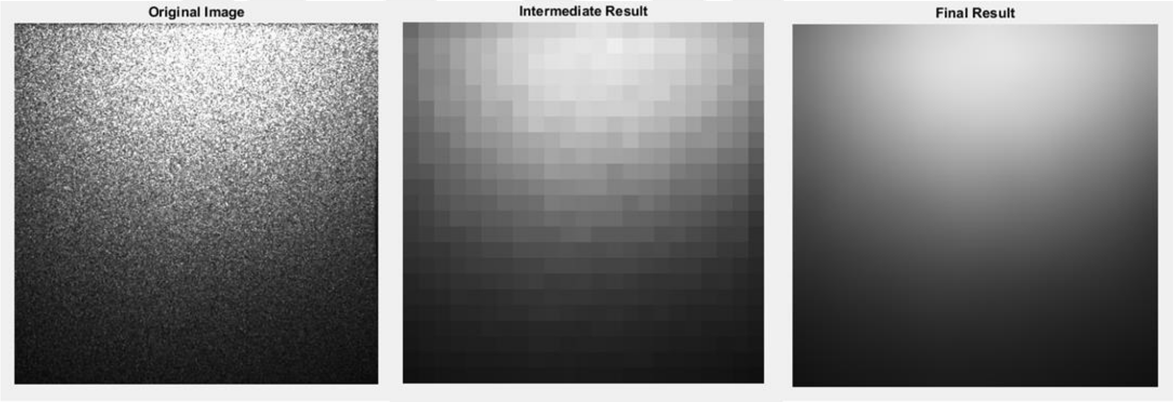

Figure 3.4. Intensity pattern used for brightness uniformity correction. The image to the left was obtained when the displayed content was a red square. A non-linear filter was used to obtain the image at the center, which was then low-pass filtered to generate the final intensity pattern (right).

The experimentally obtained intensity pattern was then used to modify the initial image so that the final image captured by the camera has brightness uniformity. By dividing the initial image by the intensity pattern before hologram calculation, a higher quality image was captured by the camera, which is shown in Figure 3.5.

Figure 3.5. Effect of correcting for brightness uniformity. The original image (left) was corrected for brightness uniformity using the intensity pattern in Figure 3.4 to obtain the image to the right.

The second major problem affecting image quality was that the image was clearly aberrated. Significant astigmatism along with defocus could be identified even when looking at the image with the eye. One of the most challenging aspects of dealing with this problem was that an interferometric system was difficult to set up, which would have been used to measure the aberration quantitatively. As an alternative, in order to correct the aberrations, the full-complex hologram was multiplied by individual Zernike polynomials with varying coefficients and the effects were observed qualitatively. Similar to the hologram computation procedure, only the first few Zernike polynomials were sufficient to correct for the majority of the aberrations. The most dominant aberrations we defocus and astigmatism, which was expected based on empirical observations. Figure 3.6 shows how correcting the aberrations improved image quality and resulted in the entire FOV being in focus simultaneously.

Figure 3.6. Effects of aberration and distortion correction. The original image (left) was corrected for aberrations to obtain the image at the center. Distortion correction was used to correct the corners of the image, resulting in the image to the right.

The final issue was that the final image was slightly distorted by the ellipsoid mirror, the left side of the FOV was magnified more than the right side of the FOV. Due to the misalignment of the ellipsoid mirror, the experimental magnification nonuniformity did not match perfectly with the one predicted by simulations. In order to fix this problem the distortion was measured by selecting a rectangular grid as the input image and observing the image captured by the camera. Then, the inverse distortion mapping was used to pre-distort the initial image, resulting in the corrected image. Figure 3.6 shows the effects of a simplified version of this procedure: only the 4 corners of the FOV were corrected using this technique, which results in the horizontal edges being parallel, but the vertical edges being slightly curved. A more sophisticated nonlinear distortion correction procedure can be applied to remove the distortion entirely.

3.3 Conclusion

A method for computing holograms for the eye-centric HWD architecture was introduced. It was shown that despite its high computational costs, the hologram can be approximated using a zone-based approach with shorter computation times, which can further be decreased using a more sophisticated optical design with uniform magnification across the FOV. As a final note, defects such as aberrations and distortion caused by alignment issues were corrected digitally by modifying the hologram.

4 EXPERIMENTAL VERIFICATION OF THE EYE-CENTRIC ARCHITECTURE

4.1 Experimental Results

In our experiments, we used Holoeye GAEA as the SLM, which is a 4K (3840x2160 pixels) LCoS phase modulator chip with 3.74 μm pixel pitch. The light source is a LASOS MCS4 series 3 wavelength fiber coupled laser with wavelengths of 473 nm, 515 nm and 639 nm for blue, green and red colors, respectively. We cut a section of the ellipsoid that gives 60° horizontal and 40° vertical FOV. The part is fabricated using diamond turning on aluminum substrate, as shown in Figure 4.1.

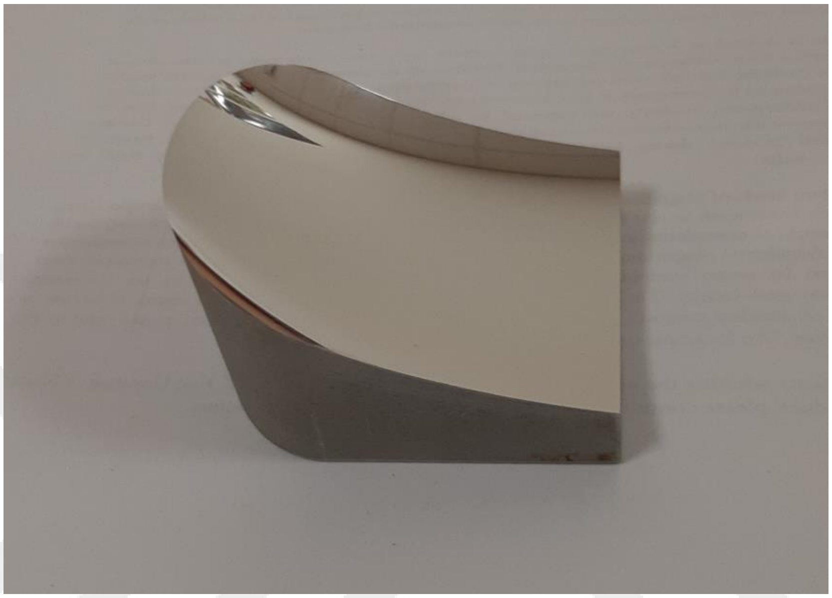

Figure 4.1. Fabricated ellipsoid mirror.

To compute the CGHs the 3D scene is modeled as a set of luminous points, similar to methods where 3D objects are represented by point clouds [30][31][32], and the hologram corresponding to the entire scene is generated by superposing the holograms for the individual points. The hologram for a single point is computed with an algorithm based on ray-tracing, which makes use of Zernike polynomials to estimate the wavefront exiting the SLM [33][34][35]. As a final step, the iterative Fourier transform algorithm is employed for phase encoding [36][37].

Figure 4.2 illustrates the experimental setup. In the optical setup, the RGB laser beam out of a single mode fiber is collimated by a lens and the collimated beam is reflected towards the SLM by a pellicle beam splitter to avoid ghost images. The incident beam on the SLM is modulated by the CGH and reflected towards the ellipsoid. The ellipsoid creates the Fourier plane at the eye pupil plane and the diffraction orders are filtered-out by the pupil. The ellipsoid also images the SLM to the rotation center of the eye and a holographic image forms on the retina. A pupil tracker camera measures the pupil position and the CGH on the SLM is updated accordingly.

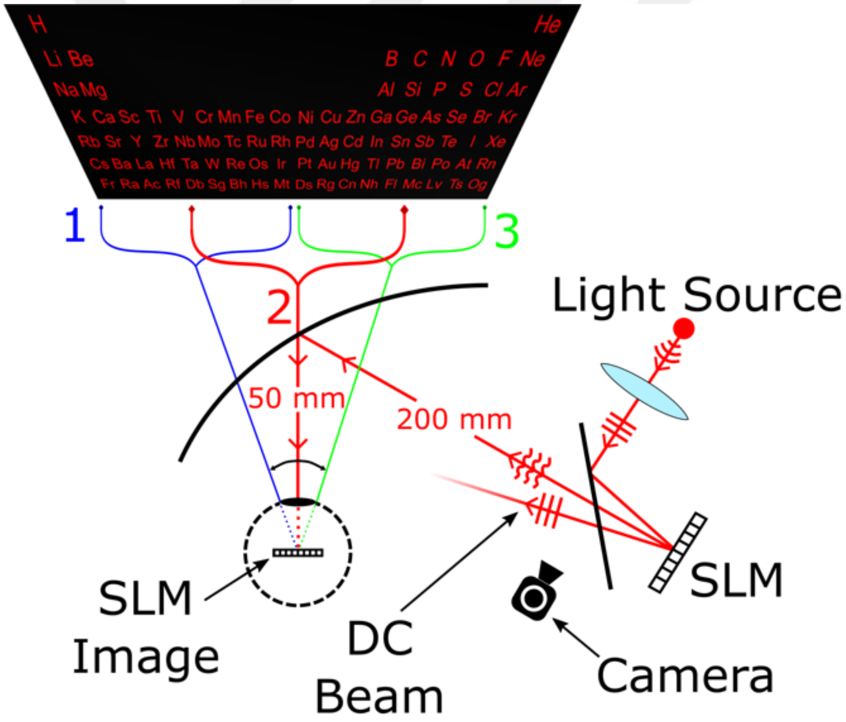

Figure 4.2. Illustration of the optical setup.

Figure 4.3 shows the experimental setup on the optical bench. As the fabricated ellipsoid is not transparent, a true augmented reality demonstration could not be made. In order to provide the peripheral image, we inserted a beam splitter between the eye and the ellipsoid and showed the low-resolution peripheral image on an LCD screen at 10 cm from the eye location without using any magnifier lenses.

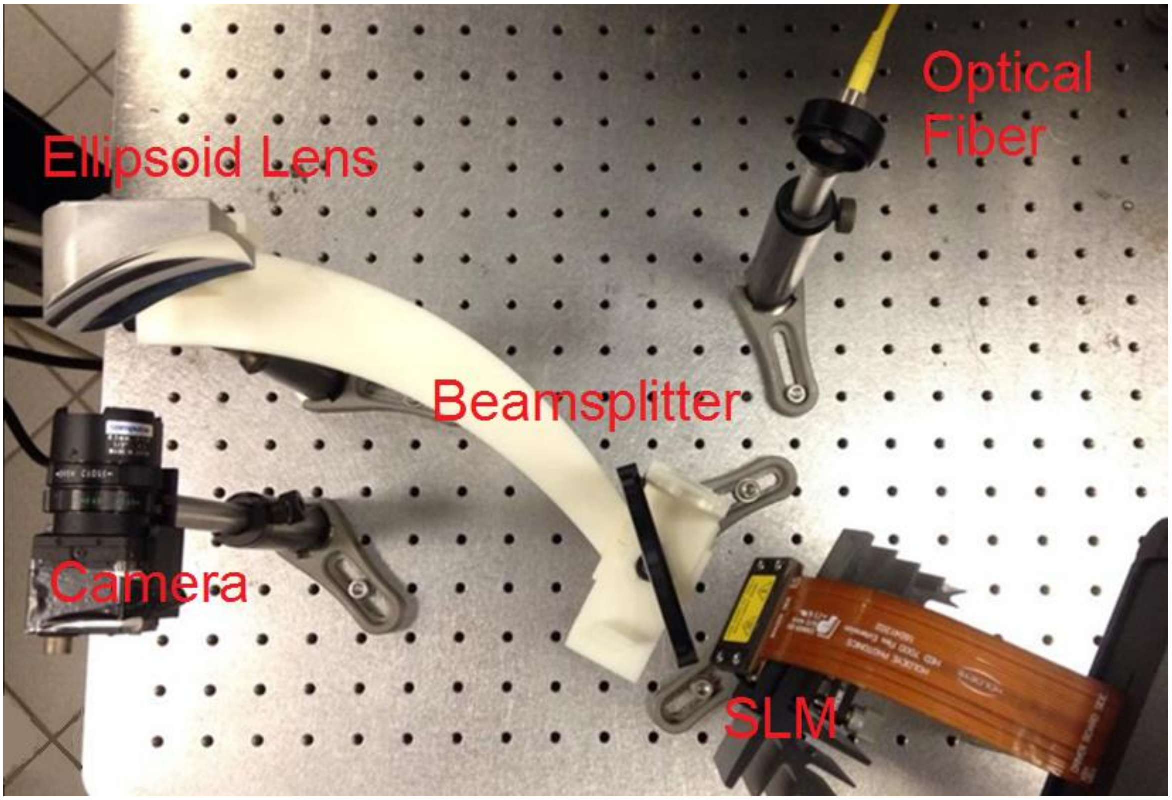

Figure 4.3. Experimental setup on the optical bench

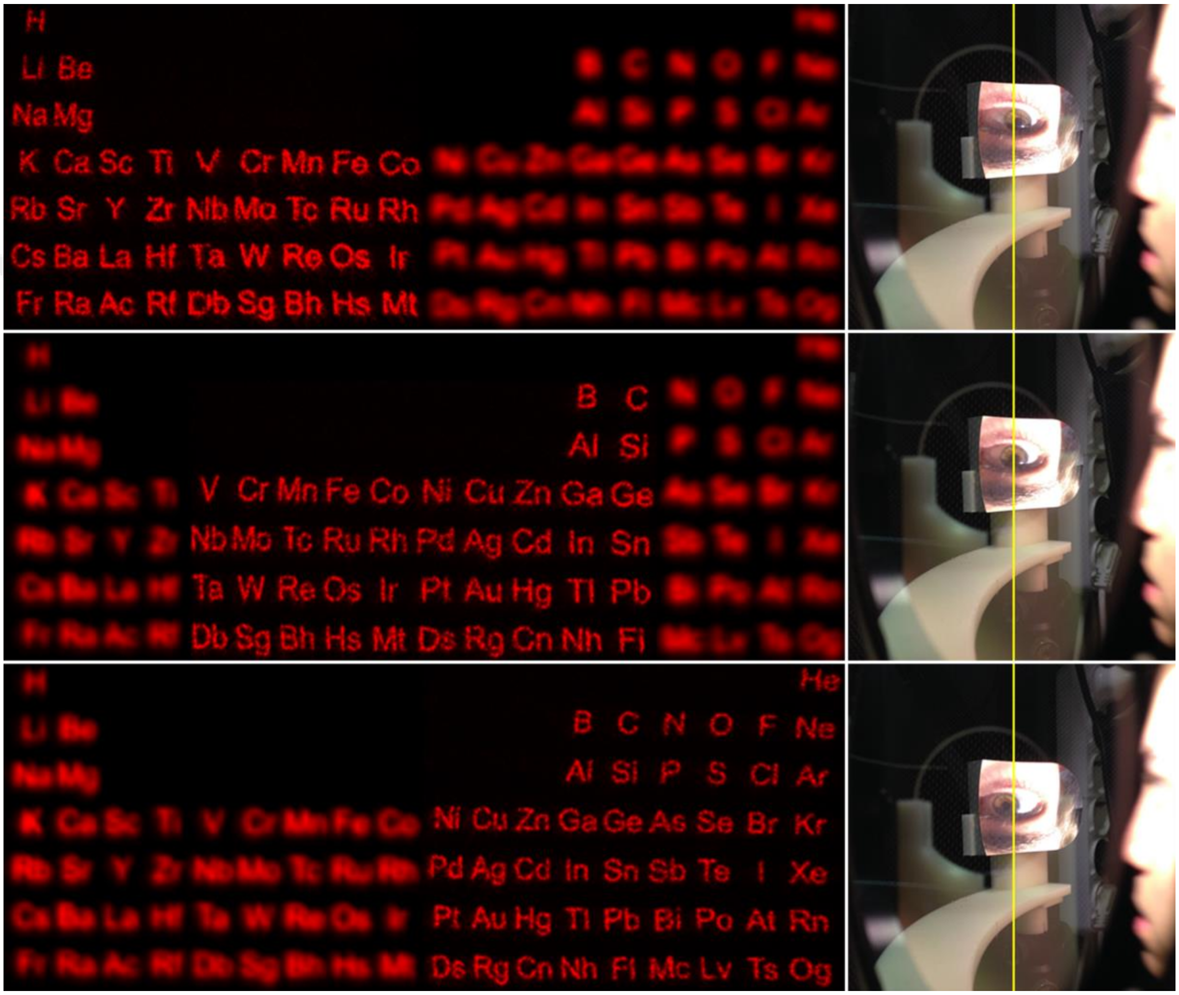

Figure 4.4. Experimental results of the eye-centric foveated holographic display. The periodic table is displayed by the SLM. As the eye rotates, a high-quality holographic view of different regions of the image is seen.

Figure 4.4 shows the experimental results for our foveated display with no moving parts. A low resolution image of the periodic table is displayed on the peripheral display at all times. The high resolution image of the viewed section is projected onto the fovea by updating the CGH on the SLM. The gaze angle is measured by a pupil tracker camera and the holograms are updated accordingly to steer the projected image. As the eye rotates, the image on the fovea remains high-resolution at all times and the rest of the image is blurred, mimicking human vision. Note the shift of pupil center with respect to the yellow reference line due to eye rotation. Despite the step change between high and low resolution regions, the human eye sees a continuous transition due to the receptor cell density variation on the retina.

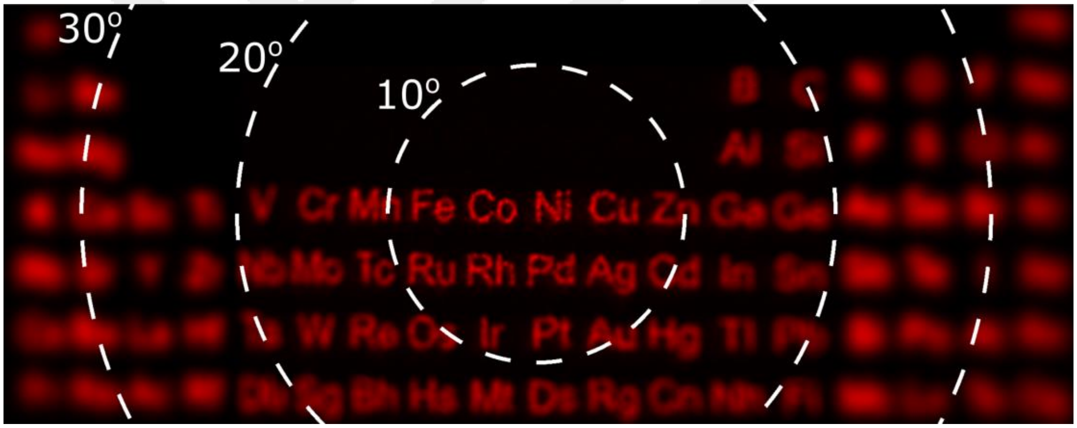

Figure 4.5. Simulation of the perceived image by the human eye. The white circles show the FOV of the eye.

Human vision was also simulated for one of the images to show the smooth transition between the high and low resolution regions, where only the resolution degradation of the human eye was taken into consideration as seen in Figure 4.5. The minimal resolvable angle size was assumed to be linearly increasing with eccentricity, which is a commonly used approximation in both vision and computer graphics [38][39]. The simulation results show that the difference between the regions generated by the holographic and the peripheral displays is not completely eliminated, but it is not as severe as the difference observed in the camera images.

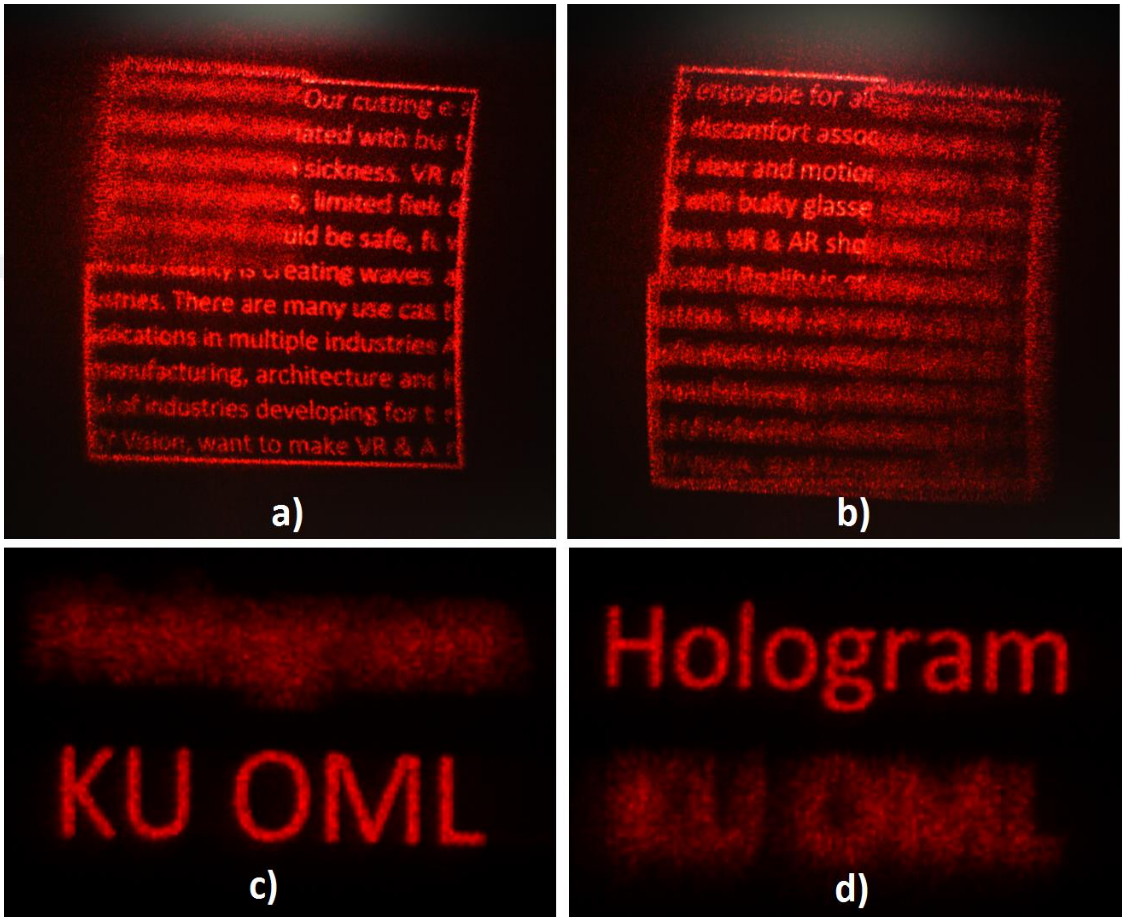

Figure 4.6. Our holographic foveated display provides continuous depth with correct focus blur.

Figure 4.6 demonstrates the capability of providing true depth information of our foveated holographic display. Objects are displayed at different depths so that only the gazed depth appears sharp, other depths appear blurred due to expected focus blur effect. Different sections of the text are displayed at different depths. In a) and b), the upper-left section of the text is displayed at 100 cm and the rest of the text is displayed at 25 cm. As the camera focus is changed, different regions appear sharp or blurred accordingly. Similarly in c) and d), top and bottom rows are displayed at 25 cm and 100 cm, respectively. Note that coherent blur appears sharper in camera images and smoother to the eye.

Color holograms can also be displayed by time-sequentially updating the CGH on the SLM and turning on the correct light source as seen in Figure 4.7. Holographic images under monochromatic illumination of wavelengths 639 nm, 515 nm, 473 nm are shown in images a) to c), respectively. Full-color image with time-sequential illumination of RGB wavelengths is shown in d).

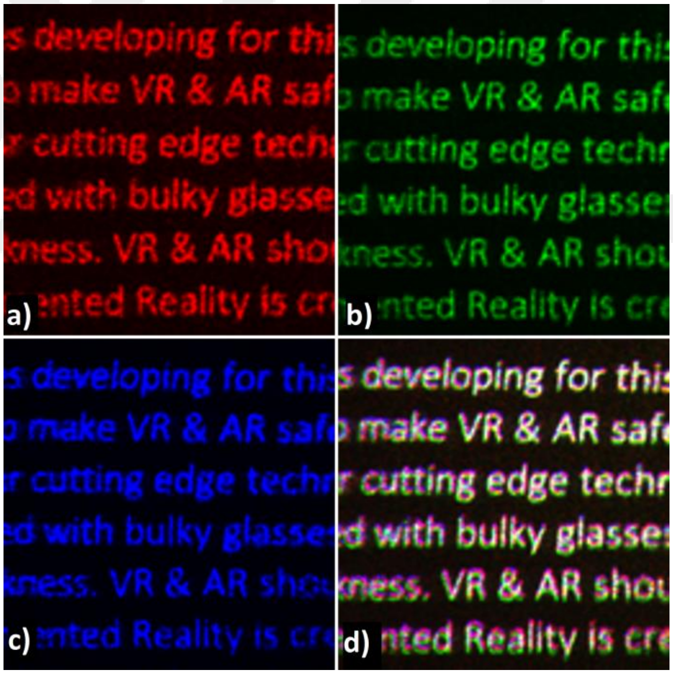

Figure 4.7. The full-color holographic demonstration. Holographic images under monochromatic illumination of wavelengths 639 nm, 515 nm, 473 nm are shown in images **a)** to **c)**, respectively. Full color image with time-sequential illumination of RGB wavelengths is shown in **d)**.

Figure 4.8. Holographic image with non-primary colors. The absence of refractive optical elements eliminates chromatic aberration, which greatly simplifies the generation of images with various color combinations.

In addition to the binary images above, it is also possible to show grayscale images using the holographic display . One such image of a succulent plant is shown on Figure 4.9 using monochromatic (red) illumination.

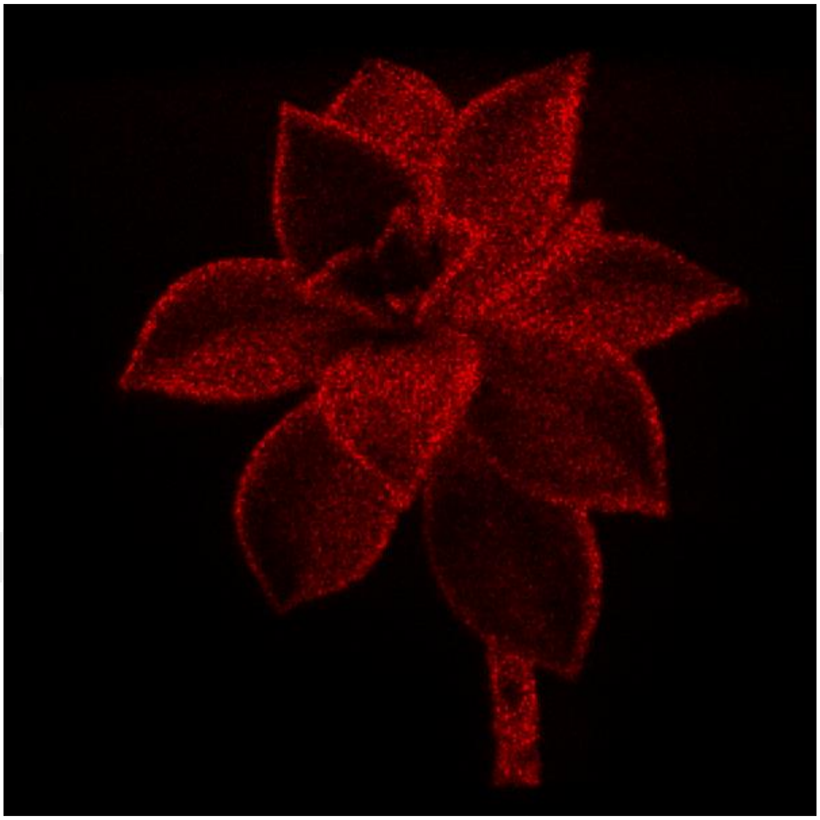

Figure 4.9. Grayscale image shown using the novel display. The speckle noise due to the initial random phase is more apparent on grayscale images, but the contrast is similar to previous experimental results.

As a final note, a 25° by 25° image consisting of a 5 by 5 array of zones is shown in Figure 4.10. The optical power was increased significantly and brightness nonuniformity was not corrected intentionally to better illustrate the shortcomings of the current display: zone transitions are evident, some zones require individual aberration correction and the background noise reduces the contrast significantly for non-sparse images.

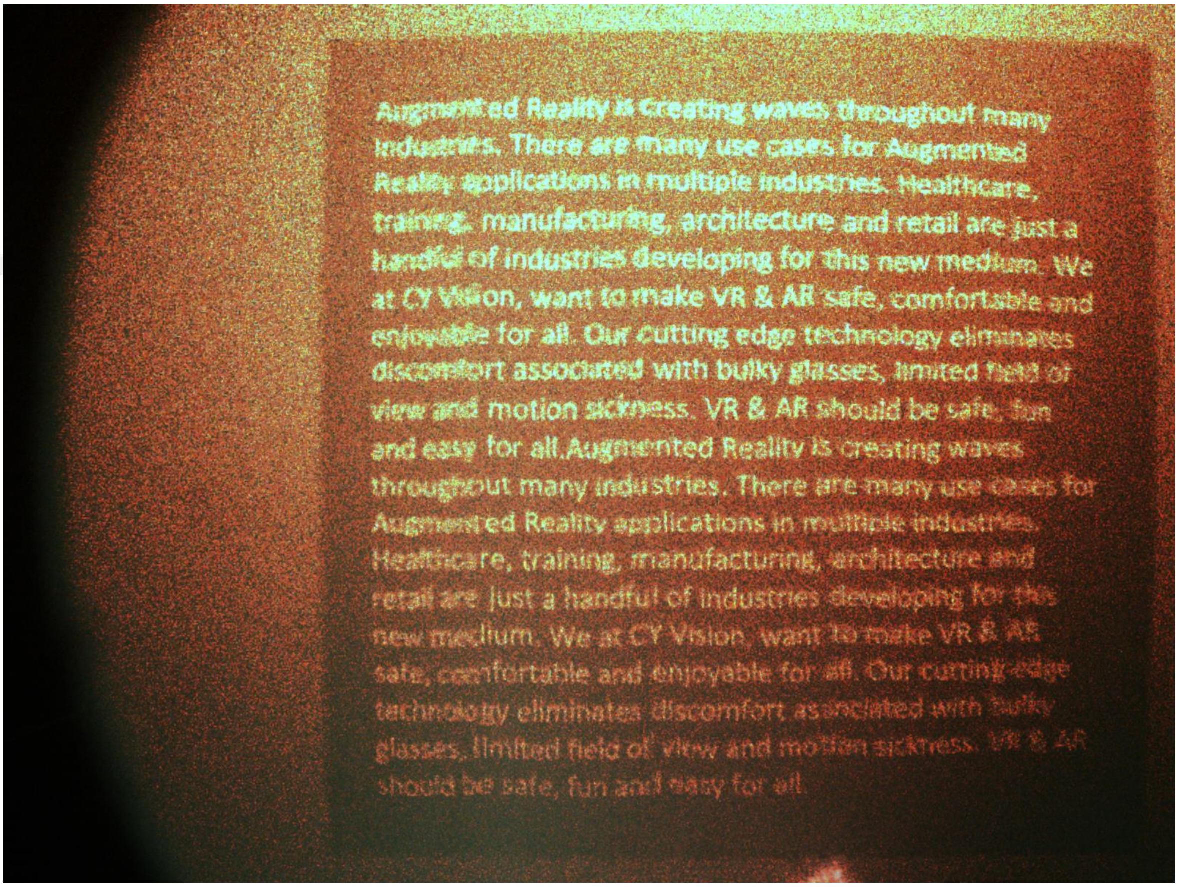

Augmented Reality is creating waves throughout many industries. There are many use cases for Augmented Reality applications in multiple industries. Healthcare, training, manufacturing, architecture and retail are just a handful of industries developing for this new medium. We at CY Vision, want to make VR & AR safe, comfortable and enjoyable for all. Our cutting edge technology eliminates discomfort associated with bulky glasses, limited field of view and motion sickness. VR & AR should be safe, fun and easy for all.Augmented Reality is creating waves throughout many industries. There are many use cases for Augmented Reality applications in multiple industries. Healthcare, training, manufacturing, architecture and retail are just a handful of industries developing for this new medium. We at CY Vision, want to make VR & AR safe, comfortable and enjoyable for all. Our cutting edge technology eliminates discomfort associated with bulky glasses, limited field of view and motion sickness. VR & AR should be safe, fun and easy for all.

Figure 4.10. Demonstration of the entire FOV of the holographic display. Note that the optical power was increased significantly and brightness uniformity was not corrected. The curvature of the ellipsoid mirror is visible on the left side of the image. The 0th and the 1st diffraction orders of the unmodulated beam are visible at the upper and lower sides of the image, respectively.

4.2 Custom Eyebox-FOV Curve Design

For a virtual image distance of infinity, it is possible to approximate the eyebox-FOV curve without performing any optical simulations. Rays coming from such a virtual image point located at a viewing angle of θ pass through the pupil and reach the SLM image plane, filling a portion of the SLM image. For sake of simplicity, assume that the SLM is perfectly imaged to the eye center and the magnification non-uniformity is negligible i.e., the SLM image is symmetric with respect to the center of the eye. Under these assumptions, the eyebox size for the point is simply the overlap area of the SLM image and the circular pupil function when the latter is shifted by $d = \tan(\theta)\, r$. In other words, convolving the circular pupil function with the 2D SLM image function in the space domain and converting to the angle domain using $\theta_x = \arctan\left(\frac{x}{r}\right)$ and $\theta_y = \arctan\left(\frac{y}{r}\right)$ results in the 2D eyebox-FOV surface.

$$EB(\theta_x, \theta_y)\big|_{\theta_x=\arctan\left(\frac{x}{r}\right), \theta_y=\arctan\left(\frac{y}{r}\right)} = SLM_i(x, y) * P(x, y) \tag{10}$$

$$P(x, y) = \begin{cases} 1, \sqrt{x^2 + y^2} < r_{pupil} \\ 0, otherwise \end{cases} \tag{11}$$

In our current experimental setup, the SLM is illuminated by a collimated laser beam with constant intensity in space, resulting in a constant SLM image function within the SLM image size. One possible way to generate SLM image functions consisting of nonnegative real numbers is to modify the illumination optics such that some parts of the SLM are illuminated more than the others. Note that any phase differences in the illumination wave due to optical path differences can be corrected by modifying the hologram on the SLM itself.

For a given pupil, it is possible to compute the SLM image function that would result in a desired eyebox-FOV surface using deconvolution algorithms. Note that the space-bandwidth product cannot be increased with this method as the number of pixels on the SLM has not changed. On the contrary, some pixels on the SLM may not be illuminated for a given custom SLM image function, resulting in a lower space-bandwidth product or a smaller volume under the eyebox-FOV surface. Nevertheless, if the space-bandwidth product is not a major concern for a system, it is possible to design a custom eyebox-FOV surface. Possible advantages include lower power consumption due to illumination and easier SLM driving schemes for SLMs with many pixels. One such example is shown in Figure 4.11, where the desired eyebox-FOV surface is a symmetric 2D Gaussian centered around the origin with a standard deviation of 10°. The required SLM image function was calculated using the Richardson-Lucy restoration algorithm[10]. The pupil radius was assumed to be 3 mm and the distance from the eye center to the pupil plane was taken as 12 mm.

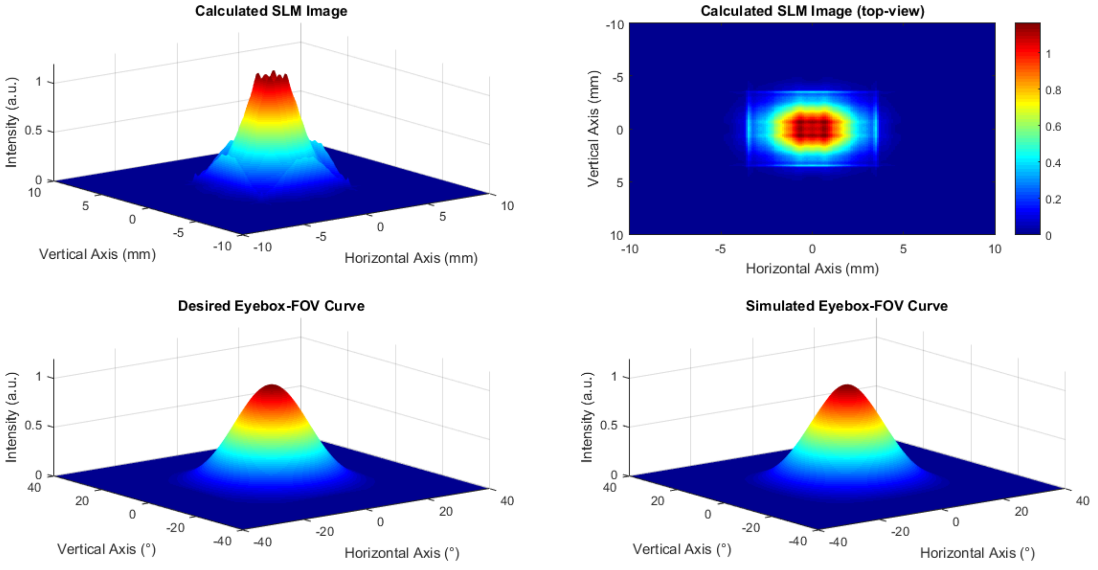

Figure 4.11. The required SLM image function (top row) was calculated for a Gaussian eyebox-FOV curve (bottom-left). The 2D convolution of the calculated SLM image with the pupil function results in the simulated eyebox-FOV curve (bottom-right).

4.3 Conclusion

The optical setup designed in Chapter 2 was realized and holograms computed using the algorithm described in Chapter 3 were used to display images, which were captured using a camera. An instantaneous FOV of 25° by 25° was demonstrated successfully. Furthermore, the instantaneous FOV was moved to the left and to the right by 10°, proving the foveated holographic display concept. A low-resolution peripheral vision display can be added for a full system implementation. ,. In addition, full-color and grayscale holograms were displayed with clear focus blur, demonstrating that the eye-centric architecture is capable of providing an instantaneous FOV similar to that of a conventional HNED.

5 CONCLUSIONS AND FUTURE WORK

In this work, we proposed the eye-centric architecture for 3D holographic HWDs, which makes it possible to steer the instantaneous FOV within a larger extended FOV without using any moving parts or dynamic optical components. Given a reflective phase-only SLM, we have developed a design procedure for an eye-centric holographic HWD and described an algorithm to compute holograms for any optical setup as discussed in detail in the supplementary material. The experimental results verify that the proposed system is able to display 3D images in a wide, steerable FOV. We achieved 28° instantaneous FOV within an extended FOV of 60×40 degrees using a 4K SLM.

With our eye-centric display demonstration, the main drawback was the aluminum ellipsoid in front of the eye, which made an augmented reality demonstration impossible. A semi-reflective ellipsoid or an HOE should be fabricated in the future to overcome this issue. Furthermore, our demonstration of a moving hologram should be integrated with a pupil tracker so that the gaze direction of the user can be estimated, which makes it possible to update the hologram automatically and make the transition between the holographic and the peripheral displays seamless for the user. Such a display would necessitate the addition of a left eye module for accurate gaze estimation and a mechanism to adjust the interpupillary distance so that the display can be calibrated for any user.

The current optical design results is very sensitive to misalignments, especially for the ellipsoid mirror and the SLM. This issue lead to the development of the aberration correction procedures described in Chapter 4, which could have been avoided altogether through better optomechanics. If more precise alignment is a possibility, adding additional optical components such as a secondary ellipsoidal mirror can provide magnification uniformity, making it possible to use a single zone-based approach instead of the multiple zone-based approach, which would greatly decrease computational costs. In addition, the hologram computation algorithms should also be further optimized and implemented with a GPU if possible in order to decrease computation times.

BIBLIOGRAPHY

[1] Rolland, J. & Cakmakci, O. Head-Worn Displays: The Future Through New Eyes. Opt. Photonics News (2009). doi:10.1364/opn.20.4.000020

[2] https://www.microsoft.com/en-us/hololens

[3] https://www.magicleap.com/

[4] Kress, B. & Starner, T. A review of head-mounted displays (HMD) technologies and applications for consumer electronics. in Photonic Applications for Aerospace, Commercial, and Harsh Environments IV (2013). doi:10.1117/12.2015654

[5] Urey, H., Chellappan, K. V., Erden, E. & Surman, P. State of the art in stereoscopic and autostereoscopic displays. in Proceedings of the IEEE (2011). doi:10.1109/JPROC.2010.2098351

[6] Lambooij, M., Fortuin, M., Ijsselsteijn, W. A. & Heynderickx, I. Measuring visual discomfort associated with 3D displays. in Stereoscopic Displays and Applications XX (2009). doi:10.1117/12.805977

[7] Hoffman, D. M., Girshick, A. R., Akeley, K. & Banks, M. S. Vergence-accommodation conflicts hinder visual performance and cause visual fatigue. J. Vis. (2008). doi:10.1167/8.3.33

[8] H. Hua and B. Javidi, “Augmented Reality: Easy on the Eyes,” *Opt. Photonics News*, 2015.

[9] S. Liu and H. Hua, “Time-multiplexed dual-focal plane head-mounted display with a liquid lens,” *Opt. Lett.*, 2009.

[10] Yaraş, F., Kang, H. & Onural, L. State of the art in holographic displays: A survey. IEEE/OSA Journal of Display Technology (2010). doi:10.1109/JDT.2010.2045734

[11] Maimone, A., Georgiou, A. & Kollin, J. S. Holographic near-eye displays for virtual and augmented reality. in ACM Transactions on Graphics (2017). doi:10.1145/3072959.3073624

[12] Slinger, C., Cameron, C. & Stanley, M. Computer-generated holography as a generic display technology. Computer (Long. Beach. Calif). (2005). doi:10.1109/MC.2005.260

[13] Kazempourradi, S., Ulusoy, E. & Urey, H. Full-color computational holographic near-eye display. J. Inf. Disp. (2019). doi:10.1080/15980316.2019.1606859

[14] http://holoeye.com/lcos-microdisplays/

[15] Macovski A. Hologram Information Capacity. J Opt Soc Amer (1970).

[16] Chen, J. S., Smithwick, Q. Y. J. & Chu, D. P. Coarse integral holography approach for real 3D color video displays. Opt. Express (2016). doi:10.1364/oe.24.006705

[17] Agour, M., Falldorf, C. & Bergmann, R. B. Holographic display system for dynamic synthesis of 3D light fields with increased space bandwidth product. Opt. Express (2016). doi:10.1364/oe.24.014393

[18] Yu, H., Lee, K., Park, J. & Park, Y. Ultrahigh-definition dynamic 3D holographic display by active control of volume speckle fields. Nat. Photonics (2017). doi:10.1038/nphoton.2016.272

[19] Häussler, R., Schwerdtner, A. & Leister, N. Large holographic displays as an alternative to stereoscopic displays. in Stereoscopic Displays and Applications XIX (2008). doi:10.1117/12.766163

[20] Rolland, J. P., Thompson, K. P., Urey, H. & Thomas, M. See-through head worn display (HWD) architectures. in Handbook of Visual Display Technology (2012). doi:10.1007/978-3-540-79567-4_10.4.1

[21] Liu, Y.-Z., Pang, X.-N., Jiang, S. & Dong, J.-W. Viewing-angle enlargement in holographic augmented reality using time division and spatial tiling. Opt. Express (2013). doi:10.1364/oe.21.012068

[22] Sando, Y., Barada, D. & Yatagai, T. Holographic 3D display observable for multiple simultaneous viewers from all horizontal directions by using a time division method. Opt. Lett. (2014). doi:10.1364/ol.39.005555

[23] Hahn, J., Kim, H., Lim, Y., Park, G. & Lee, B. Wide viewing angle dynamic holographic stereogram with a curved array of spatial light modulators. Opt. Express (2008). doi:10.1364/oe.16.012372

[24] Finke, G., Kozacki, T. & Kujawińska, M. Wide viewing angle holographic display with a multi-spatial light modulator array. in Optics, Photonics, and Digital Technologies for Multimedia Applications (2010). doi:10.1117/12.855778

[25] Kozacki, T., Kujawinska, M., Finke, G., Hennelly, B. & Pandey, N. Extended viewing angle holographic display system with tilted SLMs in a circular configuration. Appl. Opt. (2012). doi:10.1364/AO.51.001771

[26] Kim, J. et al. Foveated AR: dynamically-foveated augmented reality display. ACM Trans. Graph. (2019). doi:10.1145/3306346.3322987

[27] Goodman, J. W. Introduction to Fourier Optics, Second Edition. *Opt. Eng.* (1996). doi:10.1117/1.601121

[28] J. H. Park, “Recent progress in computer-generated holography for three-dimensional scenes,” *J. Inf. Disp.*, 2017.

[29] S.-K. Lee, S.-I. Hong, Y.-S. Kim, H.-G. Lim, N.-Y. Jo, and J.-H. Park, “Hologram synthesis of three-dimensional real objects using portable integral imaging camera,” Opt. Express, 2013.

[30] Lucente, M. E. Interactive computation of holograms using a look-up table. J. Electron. Imaging (1993). doi:10.1117/12.133376

[31] Shimobaba, T., Nakayama, H., Masuda, N. & Ito, T. Rapid calculation algorithm of Fresnel computer-generated-hologram using look-up table and wavefront-recording plane methods for three-dimensional display. Opt. Express (2010). doi:10.1364/oe.18.019504

[32] Kim, S.-C., Dong, X.-B., Kwon, M.-W. & Kim, E.-S. Fast generation of video holograms of three-dimensional moving objects using a motion compensation-based novel look-up table. Opt. Express (2013). doi:10.1364/oe.21.011568

[33] Shi, Y., Cao, H., Gu, G. & Zhang, J. Technique of applying computer-generated holograms to airborne head-up displays. in Holographic Displays and Optical Elements II 3559, 108–112 (2003).

[34] Cao, H., Sun, J. & Chen, G. Bicubic uniform B-spline wavefront fitting technology applied in computer-generated holograms. in 2nd International Symposium on Advanced Optical Manufacturing and Testing Technologies: Advanced Optical Manufacturing Technologies (2006). doi:10.1117/12.674234

[35] Li, S. et al. A practical method for determining the accuracy of computer-generated holograms for off-axis aspheric surfaces. Opt. Lasers Eng. (2016). doi:10.1016/j.optlaseng.2015.08.009

[36] Fienup, J. R. Iterative Method Applied To Image Reconstruction And To Computer-Generated Holograms. Opt. Eng. (1980). doi:10.1117/12.7972513

[37] Wyrowski, F. & Bryngdahl, O. Iterative Fourier-transform algorithm applied to computer holography. J. Opt. Soc. Am. A (1988). doi:10.1364/josaa.5.001058

[38] Strasburger, H., Rentschler, I. & Jüttner, M. Peripheral vision and pattern recognition: A review. J. Vis. (2011). doi:10.1167/11.5.13

[39] Guenter, B., Finch, M., Drucker, S., Tan, D. & Snyder, J. Foveated 3D graphics. in ACM Transactions on Graphics (2012). doi:10.1145/2366145.2366183